Progress in Oceanography 191 (2021) 102507

Contents lists available at ScienceDirect

Progress in Oceanography

journal homepage: www.elsevier.com/locate/pocean

Observational and modeling studies of oceanic responses and feedbacks to typhoons Hato and Mangkhut over the northern shelf of the South China Sea

Wenjie Dong [a], Yanqing Feng [b], Changsheng Chen [c,*], Zhongxiang Wu [c], Danya Xu [d], Siqi Li [c], Qichun Xu [c], Lu Wang [c], Robert C. Beardsley [e], Huichan Lin [c], Ruixiang Li [b], Junkun Chen [f], Jiahui Li [f]

[a] School of Atmospheric Sciences, Sun Yat-sen University, Guangzhou 510275, China
[b] South China Sea Marine Surveying and Technology Center, State Ocean Administration, Guangzhou 519399, China
[c] School for Marine Science and Technology, University of Massachusetts-Dartmouth, New Bedford, MA 02744, USA
[d] Southern Marine Science and Engineering Guangdong Laboratory, Zhuhai 519082, China
[e] Department of Physical Oceanography, Woods Hole Oceanographic Institution, Woods Hole, MA 02532, USA
[f] National Supercomputing Center in Guangzhou, Sun Yat-Sen University, Guangzhou 510006, China

ABSTRACT

Meteorological and oceanic responses to Typhoons Hato and Mangkhut were captured by storm-monitoring network buoys over the northern shelf of the South China Sea. With similar shelf-traversing trajectories, these two typhoons exhibited distinctly different features in storm-induced oceanic mixing and oceanic heat transfer through the air-sea interface. A well-defined cold wake was detected underneath the storm due to a rapid drop in sea surface temperature during the Hato crossing, but not during the Mangkhut crossing. Impacts of oceanic mixing on forming a storm-produced cold wake were associated with the pre-storm condition of water stratification. In addition to oceanic mixing produced through the diffusion process by shear and buoyancy turbulence productions, the short-time scale of mixing suggested convection/overturning may play a critical role in the rapid cooling at the sea surface. The importance of convection/overturning to mixing depended on the duration of atmospheric cooling above the sea surface-the longer the atmospheric cooling, the more significant effect on mixing. Including the oceanic mixed layer (OML) in the WRF model was capable of reproducing the observed storm-induced variations of wind and air pressure, but not the air and sea surface temperatures. Process-oriented numerical experiments with the OML models supported both observational and modeling findings. To simulate the storm-induced mixing in a coupled atmospheric and oceanic model, we need to improve the physics of vertical mixing with non-hydrostatic convection/overturning. Warming over the shelf is projected to have a more energetic influence on future typhoon intensities and trajectories.

PLAIN LANGUAGE SUMMARY

The South China Sea (SCS) is a region vulnerable extremely to tropical cyclones (TCs). Typhoons Hato and Mangkhut were the strongest TCs attacking the SCS in 2017 and 2018, respectively. Storm-monitoring network buoys with a layout along the 50-m isobath over the northern shelf of the SCS captured meteorological and oceanic responses to these two typhoons. The observations revealed that these two typhoons exhibited distinctly different features in storm-induced oceanic mixing and heat transfer, even though with similar shelf-traversing paths and intensities. A well-defined cold wake formed beneath the storm due to a rapid drop in the sea surface temperature during the Hato crossing, but not during the Mangkhut crossing. The data synthesis elucidated that impacts of oceanic mixing on forming a storm-produced cold wake were associated with the pre-storm condition of water stratification. In addition to oceanic mixing produced through the diffusion process by the turbulence shear and buoyancy productions, the short-time scale of mixing suggested that convection/overturning may be a primary physical process that rapidly cooled the sea surface. The importance of convection/overturning to mixing depended on the

* Corresponding author.
E-mail address: c1chen@umassd.edu (C. Chen).

https://doi.org/10.1016/j.pocean.2020.102507
Received 29 June 2020; Received in revised form 26 October 2020; Accepted 20 December 2020
Available online 1 January 2021

atmospheric cooling duration above the sea surface, more significant as air-cooling lasts longer. To evaluate the essential role of ocean mixing in typhoon simulation, the Weather Research and Forecasting (WRF) model was applied to simulate these two typhoons under conditions with and without an oceanic mixed layer (OML). Results indicated that including the OML in the WRF reproduced observed storm-induced variations of wind and air pressure but not the air and sea surface temperatures. Process-oriented numerical experiments with the OML models supported both observational and modeling findings. To resolve the OML and vertical mixing, a coupled atmospheric and oceanic model must improve the physics of mixing with non-hydrostatic convection/overturning. The influence of warming on typhoon intensity and pathway is projected to be more energetic in the future.

1. Introduction

The South China Sea (SCS) is a region vulnerable extremely to tropical cyclones (TCs) (Neumann, 1993; Emanuel, 2003). According to the IBTrACS database (https://www.nodc.noaa.gov/ibtracs/index.php), a total of 739 TCs struck the SCS in the past 70 years over the period 1949–2018, with an average of ~10 per year. Most of these TCs were formed in the tropical region of the Northwest Pacific Ocean and moved into the SCS initially as tropical depressions and then intensified to become severe tropical storms or typhoons (Fig. 1). They occurred in all four seasons, with super typhoons usually appearing in late summer through fall. The maximum wind records have been available since 1977, which reported five super typhoons; Tita, Dot, and Megi in October 1978, 1985, and 2010, respectively; Haiyan in November 2013 and Meranti in September 2016. The SCS has undergone three storm-intensity periods. 1977–1995 was a high-frequency period of severe or super typhoons during which the average maximum wind speed of the storms was ~55.0 m/s. 1996–2006 was the low-frequency period of moderate storms during which the average storm maximum wind speed was ~41 m/s. Especially in 1997 and 2002, the strongest storm's intensity had only a peak wind speed of ~31.0 m/s. Since 2007, the SCS has entered a high-frequency period of severe or super typhoons again, during which the average storm maximum wind speed was ~54.0 m/s. Especially in 2010, 2013, and 2016, the super typhoon's maximum wind speed reached ~62.0 m/s or higher.

A storm-monitoring system consisting of eight meteorological and oceanic buoys was established over the northern SCS, with layouts of five buoys roughly along the 50-m isobath, two buoys at the 1000-m and 2000-m isobaths over the slope within major pathways of TCs, and one buoy at the ~50-m isobath over the western shelf of Hainan Island, respectively (Fig. 2). This regional storm-monitoring system was initially set up in 2005–2006 and upgraded by adding more sensors. It is integrated with 19 tidal gauges along the coast of the SCS to form the storm-monitoring network. This network has successfully recorded key meteorological and oceanic variables near the air-sea interface during storm events since 2006, including Typhoons Hato and Mangkhut that struck the northern coast of the SCS in August 2017 and September 2018, respectively (Fig. 2).

In this paper, we have selected Hato and Mangkhut as examples to examine the short-term oceanic responses to typhoons over the northern shelf of the SCS. These two typhoons moved towards the coast with parallel trajectories, and both traversed through the buoy array over the shelf (Fig. 2). The former continued to be intensified as it entered the shelf, while the latter was not. The observational data recorded on buoys provided us with a unique opportunity to examine these two typhoon's structures and behaviors and typhoon-induced air-sea interaction processes near the sea surface. In particular, how did storm-induced vertical mixing, latent heat flux, and sea surface temperature (SST) vary with the intensity, thermal character, and duration of typhoons?

Over the SCS, numerous efforts have been made in TC researches, with publication records tracking back to the'70 s (Chen and Yin, 1979). These studies covered a broad range of subjects, including the co-relation between typhoon and El Nino (Chen et al., 2013a; Li, 1988); TC development (Wang and He, 1979); convection in TCs (Chan et al., 2004), TC genesis associated with monsoons (Wang et al., 2007) and TC-induced extreme precipitation (Qiu et al., 2019), etc. Due to the lack of

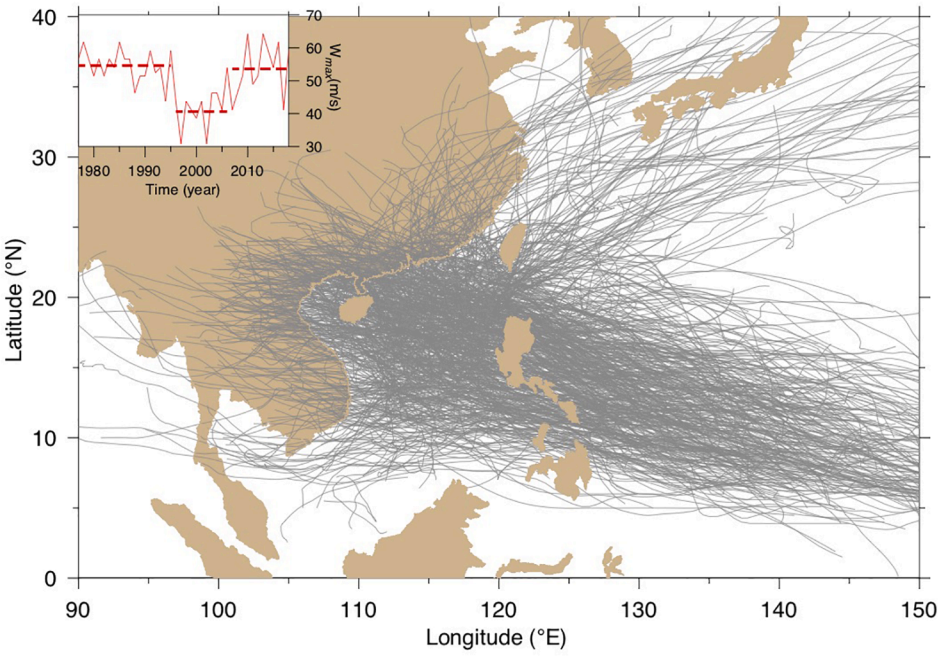

Fig. 1. Trajectories of tropical storms entering the South China Sea over the period 1949–2018. Upper-left panel represents the yearly maximum wind speed of the strong typhoon over the period 1977–2018. Red line: the maximum wind speed. Thick red dashed line: the period-averaged mean speed. The data used for this plot is from the IBTrACS database (https://www.nodc.noaa.gov/ibtracs/index.php). (For interpretation of the references to color in this figure legend, the reader is referred to the web version of this article.)

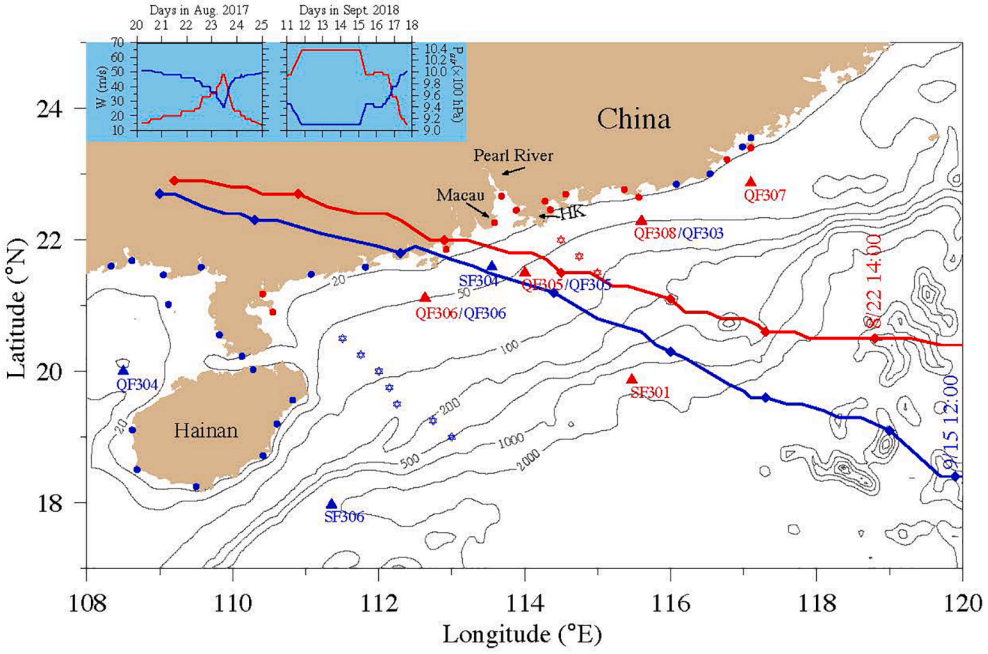

Fig. 2. Locations of buoys, hydrographic survey sites, and tidal gauges overlapping by trajectories of Typhoon Hato (thick red curve) and Typhoon Mangkhut (thick blue curve). Red solid dots: tidal gauges with water elevation records available for August 2017 and September 2018. Solid blue dots: additional tidal gauges with the water elevation records available for September 2018. Red filled triangles: the buoys named QF307, QF308, QF305, QF306, and SF301 with time-series records available in August 2017. QF303, QF305, and QF306 in blue color on some of these buoys: the buoy names used in 2018 with the time series records available in September 2018. Blue filled triangles and names of SF304, SF306, and QF304: the buoys deployed in 2018, with time-series records available in September 2018. Filled diamond symbols on typhoon trajectories: the locations of the typhoon's center over a 6-h interval. The number nearby the first diamond symbols from the right: the time with month/day and hours. Hexagram symbols: the CTD measurement sites of hydrographic surveys taken on August 12, 2017 (red) and September 20, 2018 (blue). Upper-left panels: the time series of the maximum wind (red curve) and central pressure (blue curve) of Hato (left) and Mangkhut (right). (For interpretation of the references to color in this figure legend, the reader is referred to the web version of this article.)

direct atmospheric and oceanic measurements over the continental shelf of the SCS, however, few observational and modeling studies were conducted to examine the storm-induced air-sea interaction over the continental shelf. The TCs are a major weather system for flood risk along the coast of the SCS. Early warning of coastal inundation requires an accurate prediction of the intensity, path, and landfall location of a storm as it enters the continental shelf. Since TCs can move very fast towards the coast, it is critically important to examine the short-term variability of storm-induced oceanic mixing and air-sea energy transfer over the continental shelf and their impacts on the performance of the storm forecast models.

The physics of tropical cyclones (TCs) have been well explored theoretically in the past decades. A comprehensive review of the TC's formation and development was given by Emanuel (2003). The Weather Research and Forecasting (WRF) model has become a popular mesoscale atmospheric model that has been widely used for the storm forecast in many tropical and subtropical coastal regions (https://www.mmm.ucar.edu/weather-research-and-forecasting-model). However, the performance of WRF in storm forecast differs substantially in terms of parameterizations relating to the atmosphere and marine boundary layer dynamics (Braun and Tao, 2000; Jacob et al., 2000; Fierro et al., 2009; Li et al., 2020a).

Coupling WRF with an oceanic model is a straightforward solution for improving both atmosphere and marine boundary parameterizations, especially in resolving the physics of heat energy exchanges and wind-current-wave interaction processes attributing to surface roughness at the air-sea interface. Recent studies indeed demonstrated that the air-sea interaction with oceanic feedback resulting from storm-generated cold wake could significantly influence the hurricane's intensity and trajectory (Glenn et al., 2016; Mooney et al., 2016). The cold wake at the sea surface is attributed to two physical mechanisms, 1) storm-induced vertical mixing/cooling, and 2) Ekman pumping. Storm-induced strong wind and surface cooling can produce vigorous oceanic mixing, bringing the cold water through thermoclines into the ocean mixed layer (OML). Meanwhile, the storm-induced cyclonic wind curl can move the near-surface water cyclonically and push the water away from the storm center by the Coriolis' deflection. As a result, the near-surface divergence can cause cold thermocline water to upwell towards the sea surface.

Relative contributions of storm-induced Ekman pumping and vertical mixing depend on their time scales. Pumping-induced upwelling is a latitude-dependent, vertical motion with an inertial time scale ($T_f = 2\pi/f$) (Greenpan, 1968; Frank, 1987). In the ocean, vertical mixing is caused by two major physical processes: turbulence diffusion and convection/overturning (Schlichting, 1979). The former is produced by shear and buoyancy turbulence productions with a time scale (T_D)in an order of magnitude $\sim h_m^2/A_h$, where h_m is the mixed layer depth and A_h is the vertical thermal diffusion coefficient. The latter is generally produced by the rapid cooling of the air above the sea surface through static or buoyancy instability, with a time scale (T_v)in an order of magnitude $\sim h_m/w$, where w is the vertical velocity. The storm-induced convection/overturning is a non-hydrostatic process, during which w is one or two orders of magnitude greater than the vertical diffusion rate defined as A_h/h_m. Therefore, $T_v << T_D$. Theoretically, to capture a storm-induced cold wake, especially in terms of intensity and timing, a coupled atmosphere–ocean model is required to appropriately resolve the right physics of oceanic mixing, not only vertical diffusion but also vertical convection/overturning.

As a TC moves over the sea, it gains significant heat energy from the ocean (Emanuel, 2003; Huang et al., 2009). Taking a TC as an ideal Carnot system (Emanuel, 1986), the observations revealed that the storm-induced latent heat flux was one order of magnitude greater than the sensible flux, and their relationship does not comply with the so-called Bowen's ratio (Beardsley et al., 2003; Chen et al., 2005). The

spatial and temporal variabilities of this source directly influence the intensity and trajectory of TC. The latent flux is produced by evaporation associated with the moist air density, latent heat rate of evaporation of water, friction velocity, and water vapor mixing ratio. It can be estimated by observational data recorded on surface buoys through the Monin-Obukhov Similarity Theory (Fairall et al., 1996, 2003; Edson et al., 2013). The observed latent flux can be used as an index parameter to evaluate the performance of WRF with and without ocean coupling, particularly to examine whether or not a simulated storm can reasonably or accurately produce the heat transfer from the ocean in terms of total energy, variability, and timing. A storm model fails if it cannot get the air-sea energy transfer correct, no matter how advanced the numerical technique is.

We applied WRF to simulate Hato and Mangkhut. The simulations were aimed to examine whether or not the WRF could capture the observed features on buoys. If not, what were the critical physical processes missed? The numerical experiments were done under the condition with and without the ocean mixed layer (OML). WRF includes a one-dimensional (1-D), temperature-dependent OML model developed *by* Pollard et al. (1973). Vertical mixing in these 1-D models is produced by surface wind stress and air cooling while ignoring the horizontal momentum and temperature advections. Given the initial fields of $\boldsymbol{h_m}$ and the OML-averaged sea temperature ($\overline{\boldsymbol{T}}_{oml}$), the 1-D model predicts the spatiotemporally-varying SST with the change of $\boldsymbol{h_m}$. The WRF takes oceanic feedback to the storm into account by updating the SST field at every time step. Although this approach does not encompass a fully air-sea interaction process, it does allow us to make a first-order assessment of the impact of spatiotemporally-varying SST field on storm simulations. This type of experiment should be done before a fully coupled atmosphere–ocean model is applied.

In addition, most of the primitive equation ocean models are developed based on hydrostatic assumptions in which vertical turbulence mixing is parameterized using various diffusion-based turbulent closure models (Burchard, 2002; Chen et al., 2013b; Mellor and Yamada, 1982). Coupling WRF with these ocean models does resolve vertical advection as an incompressible fluid but not convection produced by overturning (Warner et al., 2010; Li et al., 2020a,b). The fundamental questions are raised here: under what condition is a storm-induced convection/overturning required to be taken into account for storm simulations? This question has not been well explored yet in terms of observations and modeling, even though the non-hydrostatic versions of coupled atmosphere–ocean models have been available for some time (Li et al., 2020b). This paper attempts to address this question by conducting a diagnostic analysis through the SST and salinity simulation experiments using either diffusion-based or bulk instability oceanic mixing models.

The remaining sections are organized as follows. Section 2 describes the data and the model. Section 3 presents the data analysis results. Section 4 evaluates the WRF performance for typhoon simulations through comparisons with observational data. Section 5 discusses the physics of storm-induced oceanic mixing through experiments with diffusion-based and bulk-instability OML models, followed by an illustration of the potential impacts of regional warming on typhoon-induced air-sea interactions. Finally, Section 6 summarizes the conclusions.

2. Data and models

Both Hato and Mangkhut appeared initially as a tropical depression when they were in the Philippine Sea on August 19, 2017 and September 14, 2018 (Fig. 2). Hato became a tropical storm on August 20 when it entered the SCS. It reached a severe typhoon intensity with a maximum swirl wind speed of ~48.0 m/s when arriving over the northern shelf of the SCS on August 23. Two hours later, Hato made landfall at Jinwan, Zhuhai. Hato was the strongest typhoon striking the coast of Guangdong Province, China, in 2017 and was also recognized as the severest storm that has attacked Macau and Hong Kong in the past 50 years (https://en.wikipedia.org/wiki/Typhoon_Hato). Differing from Hato, Mangkhut was first intensified into a super typhoon with a maximum swirl wind speed of >65.0 m/s on its journey to Luzon, and then significantly weakened when it arrived in the SCS after traversing the mountains of Luzon. Mangkhut turned to a severe typhoon with a maximum swirl speed of ~45.0 m/s before making its second landfall at the coast of Jiangmen, Guangdong Province, on September 16 (https://en.wikipedia.org/wiki/Typhoon_Mangkhut**).** Although both Hato and Mangkhut were turned into severe typhoons and traveled through the continental shelf of the SCS with parallel trajectories, their dynamical performance significantly differed. The former was intensified with a kinetic energy gain, while the latter was weakened with a kinetic energy loss.

2.1. Observational data

The data used in this paper were from 8 buoys and two hydrographic surveys taken in August 2017 and September 2018, respectively. Since our studies were focused on oceanic responses to typhoons over the northern shelf of the SCS, the water elevation records at tidal gauges along the coast were omitted here. Each buoy was equipped with meteorological (Wind Monitor-MA-Model 05106, Relative Humidity/Temperature Probe-Model-4138LC2, Air Pressure Senor-Model-QYX4-1), and oceanic (Wave Sensor-Model-SBY1-1; Temperature Probe- Model-YQS-SW-1; AANDERAA 5800RR Current Meter) sensors to measure the wind speed and direction at a 3-m height, air pressure, air temperature and relative humidity at a 2-m height, sea temperature, water velocity and direction at a 2-m depth beneath the sea surface, and significant wave heights and peak periods. Data were generally recorded at hourly time intervals. During the period that Hato and Mangkhut passed the buoy array, the measurement time interval was changed to 0.5 h or shorter. The storm-monitoring system network was operated and maintained by the SCS Marine Surveying and Technology Center, State Ocean Administration of China. All data received from this network were processed with routine quality controls. The sensors were maintained yearly with subject to changes of locations and names of buoys. In 2017, the data on buoys QF307, QF308, QF305, and QF306, as well as SF301, were available. In 2018, QF308 was re-named QF303, and the data were available on QF303, QF305, SF304, and QF306 as well as SF306 and QF304. Due to technical malfunction, some sensors failed during the storm periods.

In 2017, a cross-isobath hydrographic survey was conducted at three sites on a transect from (114°29′53.88″E, 22°00′00.00″N) to (115°00′00.00″E, 21°30′00.00″N) near the Pearl River over the northern shelf of the SCS on August 12, about ten days before Hato arrival (Fig. 2). In 2018, a hydrographic survey was carried out at seven sites along a transect from (111°30′11.88″E, 20°29′59.64″N) to (112°59′54.00″E, 18°59′57.12″N) in the western area of the northern shelf of the SCS east of Hainan Island on September 20, about four days after Typhoon Mangkhut made landfall (Fig. 2). At each site, the temperature and salinity were recorded at 1.0-m vertical intervals by the CTD profiler.

The observed surface wind stress, latent flux, and sensible flux were calculated using the MATLAB air-sea toolbox program developed originally by R.C. Beardsley and upgraded by the user community (https://sea-mat_github.io/sea-mat/). The bulk air-sea heat flux algorithm was based on the Monin–Obukhov similarity theory with modifications for the roughness–stress relationship, boundary-layer-scale gustiness velocity, and convective limit (Fairall et al., 1996, 2003; Edson et al. 2013). This bulk algorithm compared well with direct turbulent flux measurements made in the open ocean and is widely used in coastal ocean research (Beardsley et al. 2003; Chen et al. 2005).

2.2. The WRF model and designs of numerical experiments

In this study, the typhoon simulation was conducted using the Advanced Research Weather (ARW) research and forecasting model. The ARW is an updated version of WRF with significant improvements

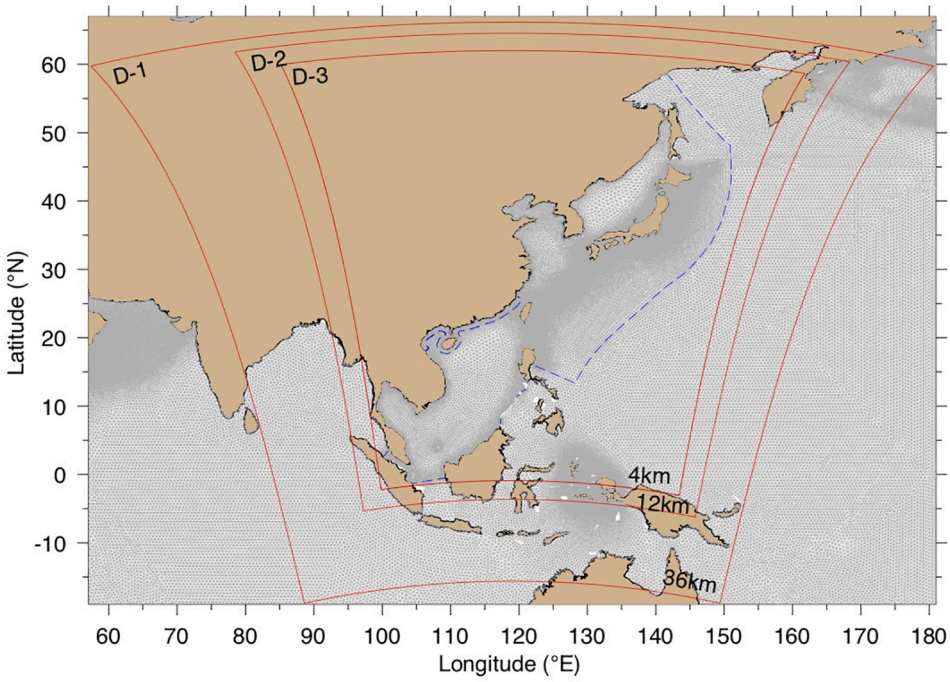

Fig. 3. Illustration of the WRF model domains overlapped over the unstructured triangular mesh of the Global-FVCOM. Symbols named D-1, D-2, and D-3 represent the three two-way nesting domains with the horizontal grid-resolutions of 36, 12, and 4 km. The horizontal grid-resolution of the Global-FVCOM in the D-3 domain varied from 2 to 5 km near the coast and over the continental slope to 25 km in the interior. Dashed blue lines indicate the nesting boundaries of Global-FVCOM/CS-FVCOM and CS-FVCOM/SCS-coastal inundation FVCOM, respectively. The meshes used in CS-FVCOM and SCS-coastal inundation FVCOM were omitted here. (For interpretation of the references to color in this figure legend, the reader is referred to the web version of this article.)

on dynamics required for the simulation and prediction of TCs (Zou and Xiao, 2000; Gopalakrishnan et al., 2006; Davis et al., 2008, Skamarock et al., 2008). The model was developed and maintained by the Mesoscale and Microscale Meteorological Laboratory (MMM) of the National Center for Atmosphere Research (NCAR). Here, to be consistent with the popular terminology used in oceanic and atmospheric literature, we refer to "ARW" as "WRF."

We have developed a Sun Yat-sen University Community Integrated Model (SYCIM). An SYCIM-based forecast system was established for the western Pacific Ocean region with a focus area on the SCS region. The regional forecast system consists of 1) WRF and 2) global-to-coastal nested FVCOM (the Finite-Volume Community Ocean Model), including *a*) Global-FVCOM, *b*) China Sea (CS)-FVCOM, and *c*) SCS-coastal inundation FVCOM. The WRF was configured by three two-way nesting domains with grid-resolutions of 36, 12, and 4 km (hereafter referring to as D01, D02, and D03) in the horizontal and a total of 41 vertical layers bounded at 50 hPa (Fig. 3). The D03 output was used to compare with the buoy data. The initial and boundary conditions were specified using the 0.5°-resolution Global Forecast System (GFS) re-analysis data (https://www.ncdc.noaa.gov). The Global-FVCOM is a fully sea-ice-wave coupled global ocean model (Chen et al., 2009, 2016; Gao et al., 2011; Zhang et al., 2016a,b; Zhang et al., 2020) with a horizontal resolution of up to ~1.0 km. The CS-FVCOM is a current-wave coupled regional ocean model with a computational domain covering the Japan Sea, Bohai/Yellow/East China Sea, and South China Sea (Fig. 3). This model was nested with the Global-FVCOM and had a horizontal resolution of up to 17 m in the SCS. The SCS-Coastal Inundation FVCOM is a land–ocean-resolving model nested with the CS-FVCOM along the 50-m isobath. This model has a horizontal resolution up to ~10 m in the river and on land.

In this study, the modeling focused on the WRF simulation to examine its performance with and without oceanic feedback. The WRF experiments were done for two cases with and without the OML, respectively. The simulations were conducted over eight days from 08:00 August 21 to 08:00 August 29, 2017, for Hato and over four days from 08:00 September 15 to 08:00 September 19, 2018, for Mangkhut. The 1-D WRF OML model developed by Pollard et al. (1973) is a purely temperature-dependent model driven by the surface wind stress and net heat flux with the shortwave irradiance penetration. Mixing in the model is generated through shear and buoyancy turbulence productions due to surface wind stress and air cooling. The model is linearized by neglecting horizontal and vertical advections in both momentum and temperature equations. We used this model for the case with the OML. The initial conditions of h_m and $\overline{T}_{oml}$were specified using the nested Global-FVCOM and CS-FVCOM forecast fields at 08:00 August 21, 2017, for Hato and 08:00 September 15, 2018, for Mangkhut. The 1-D OML model updated $\overline{T}_{oml}$ at each cell, which varied in time and space, and thus feedback to typhoons with the updated air-sea temperature difference and moisture at the air-sea interface.

2.3. The OML models for diagnostic analysis

We have selected Price-Weller-Pinkel (PWP) (Price et al., 1986) and Mellor and Yamada (MY) level 2.5 (Mellor and Yamada, 1982) OML models to assess the relative importance of convection/overturning to storm-induced oceanic mixing. The PWP is a 1-D parameter-driven OML model in which mixing is determined by the criteria of turbulences given by a bulk shear instability, including static, mixed layer, and shear-flow instabilities. Diving the water column into layers, PWP mixes the water in the two neighboring points immediately as the criteria reach. In the case of surface cooling, static instability leads to mixing over one time step without delay. In this way, it accounted for rapid mixing due to cooling-induced overturning. In this study, the PWP model was the PWP_UH_version 1.1 modified and updated by *Santiago-Mandujano* and *Lukas* at the University of Hawaii. The MY level 2.5 model (hereafter referred to as MY2.5) is a diffusion-based OML model in which mixing is determined through vertical diffusion produced by solving the turbulence kinetic and mixing-length equations. These two questions contain turbulence sources from shear and buoyancy turbulence productions, sinks due to turbulence dissipation, and res-distribution resulting from advection and diffusion. In this study, the MY2.5 was from the 1-D code of FVCOM (Chen et al., 2013b). The MY2.5 does consider cooling-induced mixing through the buoyancy turbulence production. However, mixing undergoes a diffusion process with a time scale longer than overturning. The comparison between PWP and MY2.5 could provide insights into the relative importance of cooling-induced overturning to observed rapid mixing, understanding that both PWP and MY2.5 do not directly resolve non-hydrostatic convection.

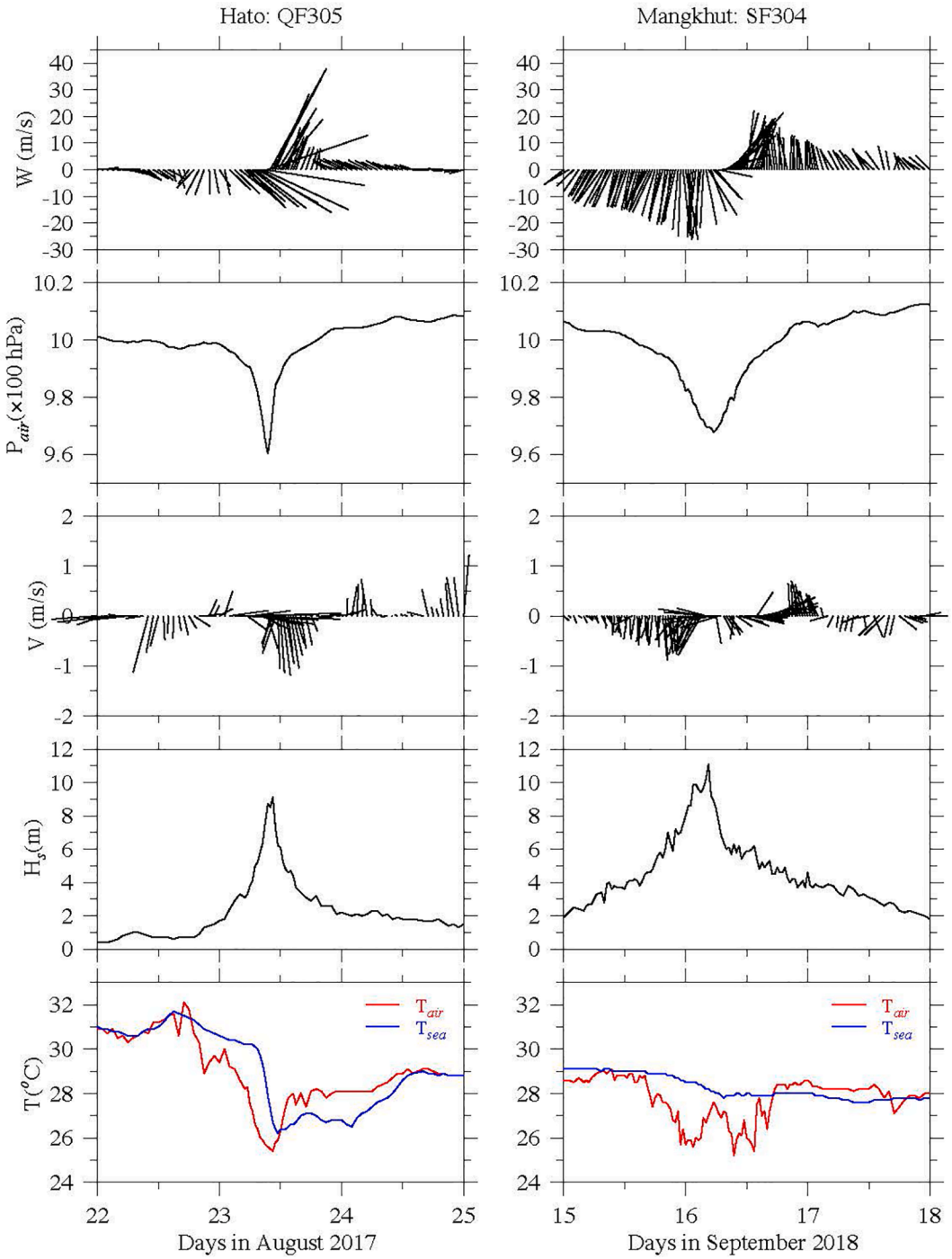

Fig. 4. Time series of wind vector (W), air pressure (P_{air}) oceanic current vector (V), significant wave height (H_s), air temperature (T_{air})and sea temperature (T_{sea}) recorded at QF305 for Hato and SF304 for Mangkhut over August 22–25, 2017 and September 15–18, 2018, respectively.

3. Observed dynamical and thermal features of Hato and Mangkhut

In August 2017, Hato traversed the buoy array consisting of QF307, QF308, QF305, and QF306) along the 50-m isobath (Fig. 2). Facing the coast, the shortest distances of these buoys to the Hato center were about 313.6 (QF307) and 147.7 km (QF308) on the right, and 41.2 (QF305) and 189.1 km (SF306) on the left, respectively. In September 2018, Mangkhut traversed the buoy array consisting of four buoys: QF303, QF305, SF304, and QF306 (Fig. 2). Facing the coast, the shortest distances of these buoys to the Mangkhut center were about 233.2 (QF303), 15.2 (QF305), and 11.1 km (SF304) on the right, and 99.4 (QF305) and 189.07 km (SF306) on the left, respectively. Although these two typhoons had similar paths towards the coast, oceanic responses at buoys significantly differed. When entering the northern shelf of the SCS, Hato was intensified, but Mangkhut was weakened, even though both were ranked as severe typhoons. Distinctly different oceanic responses were evident from the time series records of wind vector, air pressure, currents, significant wave height, air temperature, and sea temperature at buoys. To shorten the text, we selected QF305 for Hato and SF304 and QF303 for Mangkhut to highlight the main finding in the storm-induced oceanic mixing and heat energy flux, with the additional detail given in Appendix A. Also, Appendix B summarized the observed features of storm-induced surface waves.

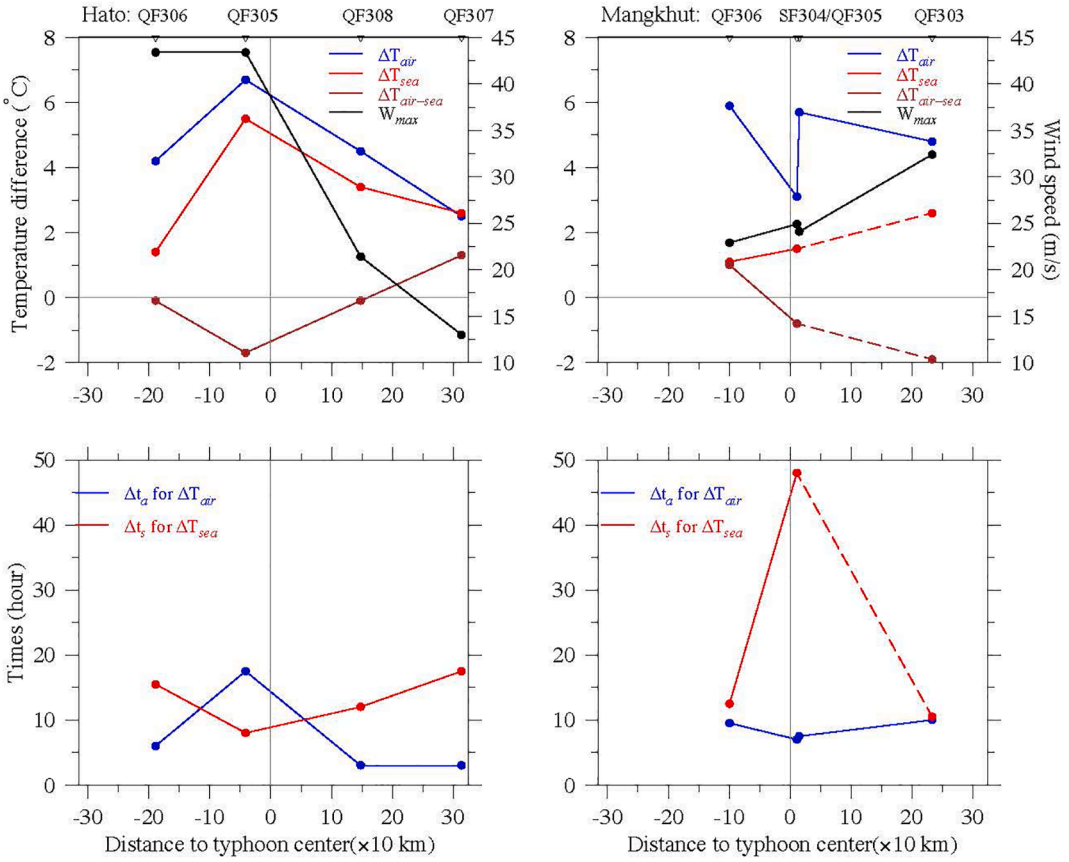

Fig. 5. Cross-typhoon distributions of the maximum drops of air and sea temperatures (ΔT_{air} and ΔT_{sea}), the difference between mean air and sea temperatures ($\Delta T_{air-sea}$) and maximum wind speed (W_{max}) over the period undergoing forΔT_{sea} (upper panel) and the times taken for ΔT_{air} and ΔT_{sea}(Δt_a and Δt_s) (lower panel) for Hato (left panel) and Mangkhut (right panel), respectively.

3.1. Storm-induced oceanic mixing

Energetic oceanic mixing was observed during Hato, but not during Mangkhut. It was evident in the sea temperature recorded at a depth of 2 m below the sea surface (Fig. 4). For Hato, at QF305, the air pressure dropped rapidly by 35.3 hPa over 31 h, starting at 02:00 August 22 and reaching 964.9 hPa (the lowest value) at 09:00 August 23. During this period, the wind near the sea surface turned cyclonic, intensified with the decrease of air pressure, and reached the maximum speed of 43.4 m/s one hour after the minimum air pressure appeared. Significant wave height increased synchronously with wind speed, with a maximum of 8.5 m coinciding with the peak wind timing. On August 22, the air-sea temperature difference was in the range of ~0.1–0.3 °C. As the Hato center approached, the air near the sea surface cooled rapidly at a rate of ~0.2 °C per hour, with a drop of 5.2 °C over 15 h. The seawater became colder as air temperature decreased, with a few hour time lag. The near-surface sea temperature decreased by 3.8 °C over 5 h, implying that intense vertical mixing occurred during the Hato crossing. For Mangkhut, at SF304, the wind speed increased as the air pressure decreased, with the wind direction changing ~180° at the time of the minimum air pressure. The minimum air pressures and peak wind coincided, with 967.7 hPa and 28.2 m/s, respectively. Although the wind was not as strong as that observed at QF305 during the Hato crossing, Mangkhut-generated maximum surface waves reached 11.1 m. Like Hato, during the Mangkhut crossing, the air temperature decreased significantly as air pressure decreased, with a maximum drop of 3.9 °C at SF304. However, the near-surface sea temperature did not drop substantially like air temperature, even though the air was much colder than the sea. Considering Hato and Mangkhut struck the northern shelf of the SCS with comparable intensities within less than one month, why did one exhibit a significant drop in the near-surface sea temperature, but the other did not?

We calculated the maximum drops of air and sea temperatures (ΔT_{air} and ΔT_{sea}) at each buoy during the Hato and Mangkhut crossing (Fig. 5, Figs. A1 and A2 in Appendix A). Here Δt_a and Δt_swere the times taken for ΔT_{air}andΔT_{sea}, respectively, whereas $\Delta T_{air-sea}$ and W_{max} were defined as the difference between mean air and sea temperatures and the maximum wind speed over Δt_s, respectively. For Hato, $\Delta T_{sea}(\Delta T_{air})$ was the largest at QF305, which was 4.1 (2.5), 2.9 (4.2), and 2.1 (2.2)°C larger than $\Delta T_{sea}(\Delta T_{air})$ at QF306, QF307, and QF308, respectively. A well-defined cold-wake was evident underneath Hato. The fact that $\Delta T_{air-sea}$was −1.7 °C at QF305 but was close to or higher than zero at QF306, QF308, and QF307 implied that cooling-induced unstable interface condition varied across Hato, stronger within the maximum wind zone but weakened or even vanished in the outer area. The unstable interface condition can cause convection/overturning, intensifying vertical mixing at QF305. It explained why ΔT_{sea} was the largest at that site. The contribution of convection/overturning to mixing was also perspicuous by comparing ΔT_{sea}, $\Delta T_{air-sea}$, and W_{max} at QF305 and QF306. W_{max} at these two sites had the same order of magnitude, but ΔT_{sea} was much smaller at QF306. Convection/overturning tended to shorten the mixing time scale, which was elucidated in Δt_s. Δt_s was 8 h at QF305, which was about 7.5, 9.5, and 4.0 h shorter than Δt_s at QF306, QF307, and QF308, respectively. In fact, at QF305, following a significant decrease in air temperature, a rapid drop in sea temperature occurred within 4 h (Fig. 4). It suggested that convection/overturning happened in a short-time period during mixing. Convection/overturning also seemed to be relevant to Δt_a, stronger as Δt_a was longer (QF305) and weaker or even vanished as Δt_a was shorter (QF306, QF307, and QF308).

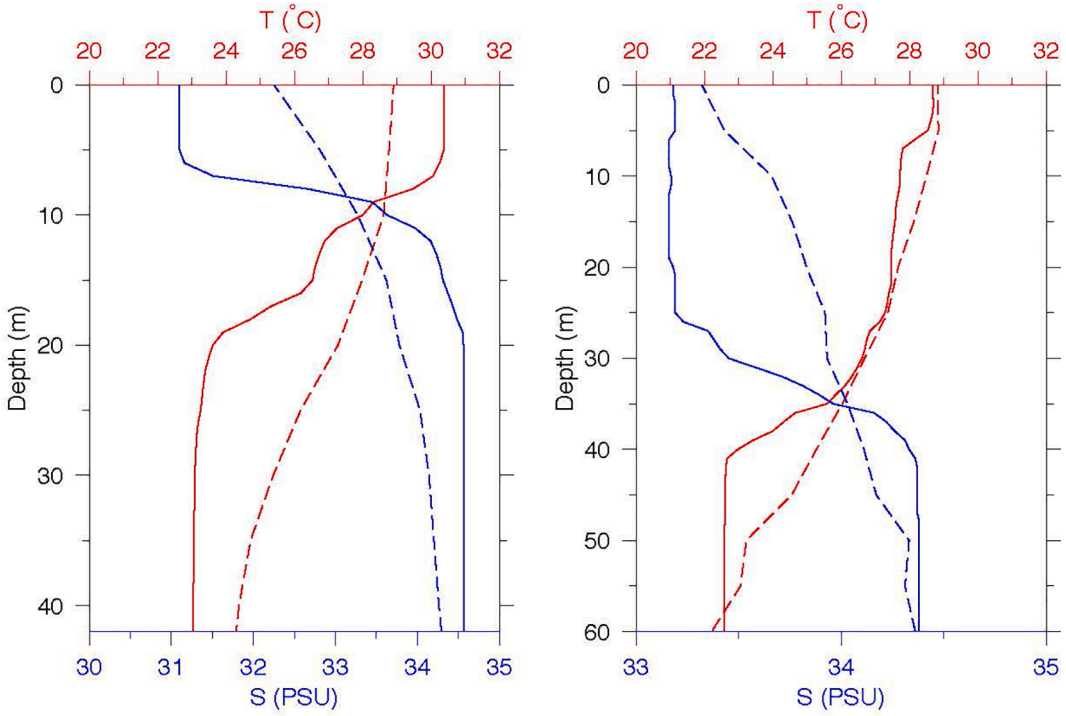

Fig. 6. Comparison of August 2017 and September 2018 in-situ temperature (*T*) and salinity (*S*) profiles with August (left) and September (right) monthly climatologically averaged profiles at the hydrographic survey sites (see Fig. 2) over the northern shelf of the South China Sea. Solid lines: in-situ; dashed lines: monthly-climatologic. Red: temperature and blue: salinity. (For interpretation of the references to color in this figure legend, the reader is referred to the web version of this article.)

For Mangkhut, ΔT_{air} was in the range of 4.8–5.9 °C at QF306, SF305, and QF303, except at SF304 where ΔT_{air} was 1.7–2.8 °C smaller. Δt_a at four sites were very close, suggesting that air cooling happened during the same period. Regarding the distance to the Mangkhut center, SF304 and QF305 were close, and both were within the same wind intensity zone. $\Delta T_{air-sea}$ was negative at SF304 and QF303, suggesting that these two sites were under a condition in favor of convection/overturning. W_{max} was ~24.9 and 32.3 m/s at SF304 and QF303, respectively, which were all strong enough to produce energetic oceanic mixing. The fact that Δt_s was 48 h at SF304 indicated that either convection/overturning or wind-induced shear turbulence production had no significant influence on a slower change of sea temperature at that site. At QF303, a 2.6 °C drop was shown in ΔT_{sea} within a period of Δt_s = 10.5 h, implying that sea surface cooling did occur at that site due to wind- and cooling-induced mixing. At QF306, the seawater remained colder than the air, i.e., $\Delta T_{air-sea} > 0.0$ and W_{max} was 22.9 m/s, so that under such a stable interface condition, mixing was generated by the wind-induced shear turbulence production. However, no significant change in the near-surface sea temperature was observed (Fig. A3). Compared with Hato, the observation did not show a well-defined cold-wake underneath Mangkhut.

We found that the distinctly different impacts of storm-induced mixing on the sea surface temperature (SST) during Hato and Mangkhut were related to the pre-storm condition of water stratification. The CTD profilers showed that the OML was much shallower in August 2017 than in September 2018 (Fig. 6), with the thicknesses of ~5 and ~25 m, respectively. The thermoclines were also thinner in August 2017 than in September 2018, which were in the range of ~5 and ~15 m, respectively. For Hato, since the pre-storm OML was shallower, once the OML produced by wind- and cooling-induced vertical mixing was deeper than 10 m, deepening of the OML could bring the cold water upward to cause a significant temperature drop at the sea surface. For Mangkhut, however, the observed OML was much deeper, so that the considerable change of SST could occur only when the mixing-produced OML was deeper than 30–40 m. This finding explained why a well-defined cold wake was observed underneath Hato but not evident underneath Mangkhut.

We also collected historical temperature (*T*) and salinity (*S*) data from the past hydrographic surveys over the northern shelf of the SCS as far back as the '60s and created the monthly climatologically fields of temperature and salinity with a 10-km horizontal resolution (Yi, 2020; Yi et al., 2020). A large portion of the historical data was obtained by measurements at selected standard levels with a vertical resolution insufficient to resolve the OML. Despite this shortcoming, the comparison of the in-situ and monthly climatological mean temperature and salinity profilers showed that the near-surface water was much warmer and fresher in August 2017 (Fig. 6). In September 2018, although the near-surface water temperature was close to the climatology, it was much fresher (Fig. 6). In recent years, the freshening and warming tendencies over the northern shelf of the SCS implied that the storm-induced air-sea interaction was more energetic compared with the past.

3.2. Storm-generated energy transfer

Using the observed data, we estimated the storm-induced latent and sensible heat fluxes at all buoys during August 22–25, 2017, for Hato, and September 15–18, 2018, for Mangkhut (Fig. 7). The results showed that the ocean provided Hato and Mangkhut with significant latent and sensible heat fluxes. Storm-generated maximum latent flux was generally 3 or 4 times greater than the maximum sensible flux. For Hato, the observed latent flux changed positively with wind speeds. At QF305, for example, the observed latent and sensible heat flux losses were approximately around zero under a wind condition of <10 m/s before Hato arrived but increased to 507.2 and 145.1 W/m^2, respectively, as the wind was intensified to 43.4 m/s over the subsequent 13-hour period during the Hato crossing, and then returned to the pre-storm condition over 4 h as the wind rapidly decreased after the passage of Hato. Mangkhut also exhibited a significant transfer of latent and sensible heat fluxes from the ocean to a storm, but differed concerning the temporal and spatial variabilities. At QF303, for example, the Mangkhut-

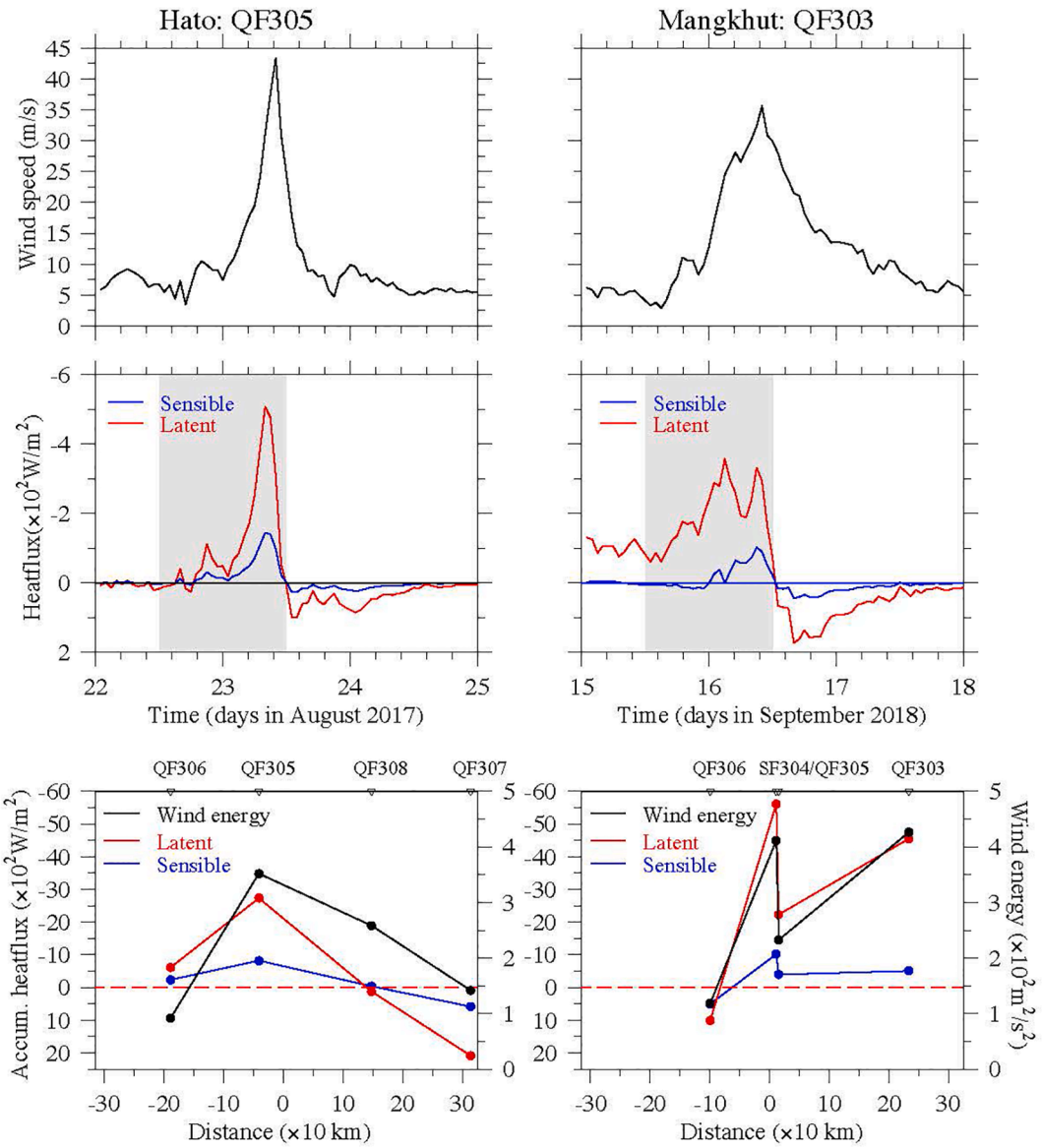

Fig. 7. Upper and middle panels: Time series of observed wind speed and sensible/latent heat fluxes over August 22–25, 2017 for Hato (left) and September 15–18, 2018 for Mangkhut (right). The shaded area is the day during which the accumulated heat fluxes and wind kinetic energy were estimated. Lower panels: Cross-typhoon distributions of the accumulated wind kinetic energy and sensible/latent heat fluxes for Hato (left) and Mangkhut (right).

generated maximum latent and sensible heat fluxes reached 358.0 and 102.7 W/m^2, respectively. They were on the same order of magnitudes as those observed at QF305 during Hato's crossing, but the transfer of latent flux to the atmosphere started under a weaker wind condition of ~5 m/s before Mangkhut arrived.

We estimated the daily accumulated wind kinetic energy and latent and sensible heat fluxes at all buoys. For Hato, the transfer of oceanic latent and sensible heats significantly varied across the typhoon: losing to the storm at QF305 and QF306, while gaining from the storm at QF307, with the transition at QF308. This distribution was not correlated to the total wind kinetic energy. On the one hand, the wind kinetic energy was the largest at QF305, cooccurring with the maximum transfer of latent and sensible heats to the typhoon at that site. On the other hand, the wind kinetic energy was larger at QF307 than at QF306, but the latent and sensible heat energies were transferred to the ocean at QF307, but to the typhoon at QF306. For Mangkhut, although the observed wind intensities were much weaker at SF304 and QF303 than at QF305 during Hato, the intense wind duration was much longer. As a result, the daily accumulated wind kinetic energies at these two sites were ~1.2 times as large as that observed at QF305 during Hato. The daily accumulated latent and sensible heats were transferred to the typhoon at SF304 and QF303 but gained from the typhoon at QF306. The maximum heat transfer to the typhoon occurred at SF304, even though the daily accumulated wind energy was larger at QF303.

The cross-typhoon distribution of heat flux was significantly asymmetrical relative to the Hato and Mangkhut centers. Hato gained the heat energy over an area bounded by a distance of 190 km on the left side and of ~147 km on the right side. Mangkhut gained heat energy over an area bounded by a distance of >233 km on the right side but only by a distance of 90 km on the left side. Capturing the spatially asymmetrical distribution of heat transfer from the ocean to a storm could directly help improve the marine boundary parameterization for coupled atmosphere–ocean models for storm-related predictions.

4. WRF simulations of Hato and Mangkhut

4.1. Typhoon simulations

We applied WRF to examine whether this model can capture the dynamic and thermal features observed during Hato and Mangkhut. By

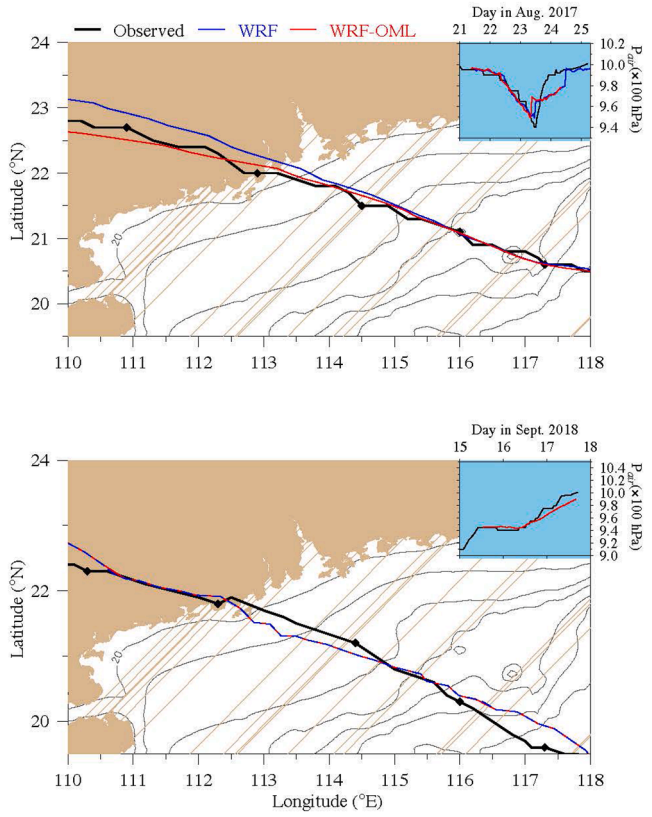

Fig. 8. Comparisons of the observed with the WRF-simulated trajectories in the case with and without the OML for Typhoon Hato (upper panel) and Typhoon Mangkhut (lower panel). The upper-right panel in each figure shows the comparison between observed simulated central minimum pressures. Black: observed; blue: WRF (without the OML).; red: WRF-OML (with the OML). Filled diamond symbols on typhoon trajectories: the locations of the typhoon's center over a 6-h interval. (For interpretation of the references to color in this figure legend, the reader is referred to the web version of this article.)

comparing the cases with and without the OML, we first verified the OML mixing impact on typhoon simulation and then explored the critical needs for model improvements. A Taylor diagram in Appendix C summarized the statistics of the model-data comparison. The results showed that WRF was robust to simulate the trajectories and central sea-level pressures of Hato and Mangkhut (Fig. 8). Including the OML dynamics did show an improvement for the Hato moving path but not for Mangkhut. Hato continued to intensify as it entered the northern shelf of the SCS and moved towards the coast. The model reproduced the drop-to-rise process of central sea-level pressure but considerably underestimated its minimum. The simulated and observed minimum central sea-level pressures occurred at 11:00 August 23, but the simulated value was about 8.8 hPa greater. Mangkhut experienced a weakening period after entering the SCS. The model captured the minimum central sea-level pressure, not only in magnitude but also in its increase rate.

The detailed data-model comparisons were made for winds, air pressure, and air temperature at buoys for Hato (Fig. 9) and Mangkhut (Fig. 10). For both typhoons, the simulated and observed winds matched well in temporal variations of wind direction but not in magnitude at buoys. For example, at QF305, Hato-generated maximum wind speed was 43.4 m/s, while the simulated maximum wind speed was only 27.7 m/s for the case without the OML and 29.3 m/s for the case with the OML. The underestimation was up to 36.2 and 32.5% for the cases without and with the OML, respectively. Including the OML did provide the wind intensity, but it only accounted for 3.7%.

Similarly, at the same site, Mangkhut-generated maximum wind was 31.9 m/s. In comparison, the simulated wind was 27.1 m/s for the case without the OML and 29.2 m/s for the case with the OML, about 15.0 and 8.5% underestimated. Including the OML accounted for a 6.5% improvement in wind intensity. For Hato, QF305 was around the maximum wind radius, whereas QF307, QF308, and QF306 were outside the maximum wind zone. The wind was underestimated at QF307 and QF308 locating on the right side of Hato and overestimated at QF306 locating on the left side of Hato. This feature implied that the model did not resolve the observed asymmetric distribution of the Hato's wind, which was stronger on the right side than on the left side. For Mangkhut, the wind intensity was much stronger at QF305 than at SF304, even though the difference in the distance to the typhoon center at these two sites was only 4.1 km. With a horizontal resolution of ~4 km, WRF could resolve the spatial variation of the wind. It was evident at SF304, where both observed and simulated maximum winds had the same value and coincided. QF306 and QF303 were about 189.07 km on the left and 233.0 km on the right. The observed maximum wind was 6.4 m/s stronger at QF303 than at QF306. The fact that the underestimation was larger at QF303 than at QF306 suggested that WRF captured neither the wind intensity nor the asymmetric distribution of the Mangkhut wind.

The model was capable of reproducing the temporal variation of air pressure at buoys over the shelf, not only the minimum pressure but also timing during the Hato crossing. However, it overestimated the minimum air pressure and caused the time delay during the Mangkhut crossing. For Hato, the difference between simulated and observed minimum air pressures was 0.4, 0.7, and 3.2 hPa at QF307, QF308, and QF306, respectively. Compared with these three sites, the model remarkably underestimated the air pressure at QF305, at which the difference between simulated and observed minimum air pressures was up to 7.5 hPa. Including the OML did provide a certain level of improvement in air pressure simulation at this site, but it only accounted for an error reduction of 5.3%. For Mangkhut, the model-data differences of minimum air pressure were 22.0, 5.4, 10.7, and 2.6 hPa at QF306, SF304, QF305, and QF303, with time delays of 4.0, 1.0, 2.0, and 0.0 h, respectively. With the OML, the differences dropped to 14.0, 3.8, 9.6, and 0.9 hPa, with improvements of 36.4, 29.6, 10.3, and 65.4% at QF306, SF304, QF305, and QF303, respectively. Although the improvements were more significant in the Mangkhut case than in the Hato case, the model-data bias remained larger in the Mangkhut case.

The model captured the significant air temperature drop during the Mangkhut crossing but not during the Hato crossing. For Hato, the model over-predicted air temperature in the outer storm area at QF306 and QF307, where the simulated air temperature was about 1.0° or 2.0 °C higher than the observed air temperature. The error was reduced significantly within a 150-km radius from the Hato center. QF305 and QF308 were located in this region, where the model did reproduce the same level of air temperature as observations. However, the model underestimated the rapid drop in air temperature, with biases of 0.7 °C at QF308 and 2.1 °C at QF305. Including the OML did not significantly improve the air temperature simulation except to a certain degree of smoothing out sharp fluctuations. For Mangkhut, the observed and simulated air temperatures were in reasonable agreement, not only in the daily mean but also in the anomaly, even though the simulated minimum air temperature was 1.0–1.5 °C higher than the observations. Including the OML did not significantly improve the air temperature simulation except filtering out the high-frequency fluctuations.

We plotted the distributions of wind speed and sea-level pressure across the storm center when Hato and Mangkhut were traversing through buoys (Fig. 11). Simulated winds were asymmetrically distributed to the central sea-level pressure, stronger on the right side. For Hato, the maximum wind radius was ~50.0 km on the right and ~46.0 km on the left. The radius on the left coincided nicely with the observed wind at QF305, suggesting that this site was located at the maximum wind zone during the Hat crossing. In this case, the distribution and values of the simulated and observed sea-level pressures and wind speeds matched reasonably well with each other. For this typhoon,

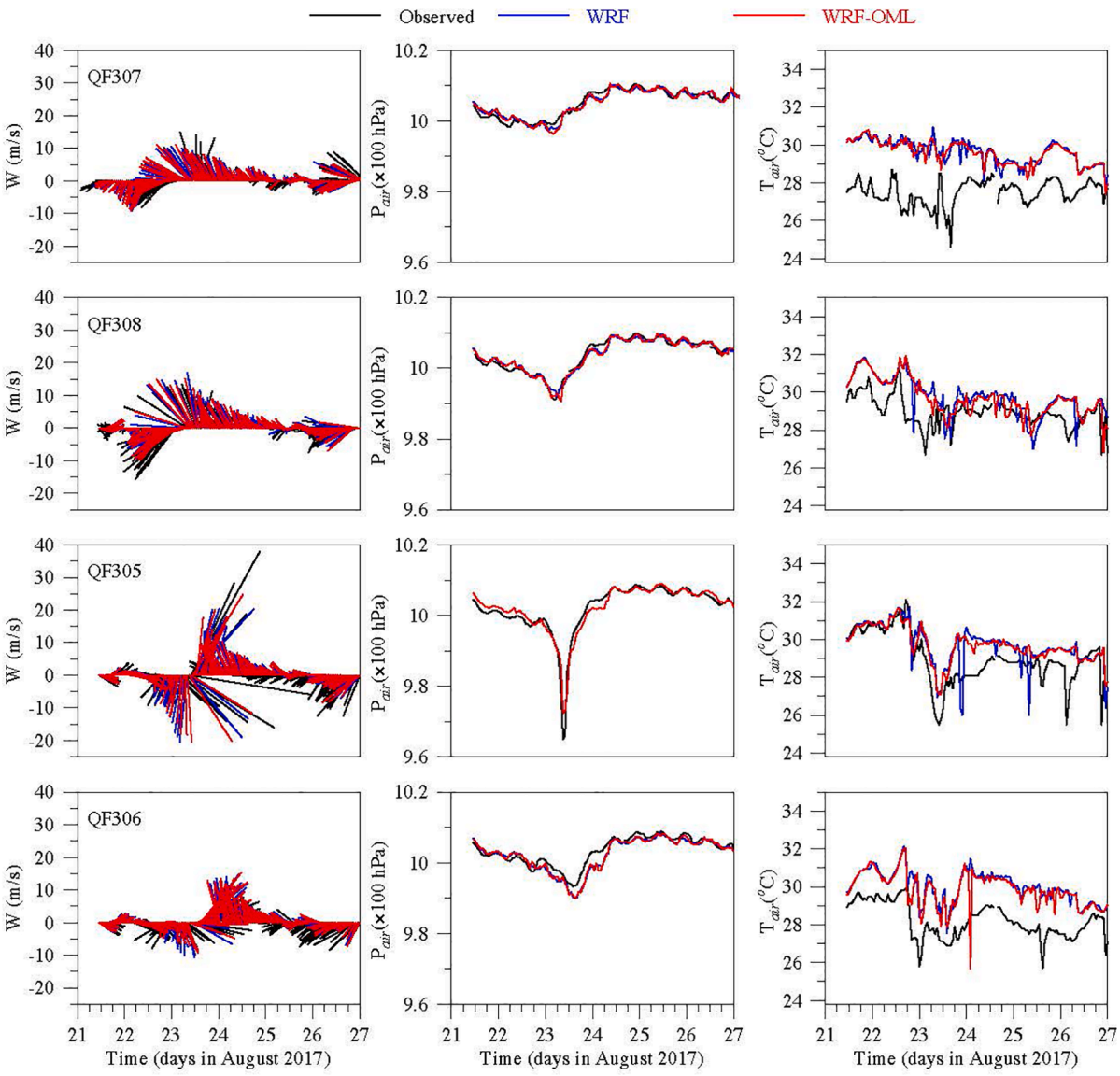

Fig. 9. Comparison between observed and simulated wind vectors (W), air pressures (P_{air}), and air temperatures (T_{air})at QF307, QF308, QF305, and QF306 over August 21–27, 2017, respectively. Black: observed; blue: WRF (without the OML); red: WRF-OML (with the OML). (For interpretation of the references to color in this figure legend, the reader is referred to the web version of this article.)

whether or not including the OML did not show the significant differences in wind and air pressure distributions. For Mangkhut, the maximum wind radius was about ~100 km on the right and ~25 km on the left. Compared with Hato, the structure of this typhoon was much more asymmetric. The model significantly underestimated the decrease rate of winds near the center of the minimum air pressure on the left and overestimated the minimum air pressure in the Mangkhut center areas. This overestimation was not improved after including the OML, even though the wind errors were considerably reduced.

4.2. Air-sea boundary conditions

Two shortcomings of WRF for storm simulation are to resolve 3-D turbulences within the storm and marine boundary parameterizations at the air-sea interface. Approaches to solving these problems are to upgrade the WRF through the implementation of the Large Eddy Simulation (LES) (Moeng et al., 2007) and coupling with current-wave interaction ocean models (Warner et al., 2010; Li et al., 2020b). In terms of air-sea coupling, it is critical to capture the nature of storm-induced oceanic turbulent mixing. Evaluating the capability of WRF to simulate the changes in sea surface temperature (SST) and latent/sensible heat fluxes can provide insights into the primary reasons why including the OML did not show a significant improvement for WRF-simulated Hato and Mangkhut.

Taking QF305 and QF303 as examples for Hato and Mangkhut, respectively, we assessed the capability of WRF on simulating the storm-induced SST (Fig. 12). Since the observed mixed layer depth was deeper than 5.0 m in August 2017 and September 2018, we can treat the sea temperature, recorded at the 2-m depth below the sea surface at these two buoys, as SST. In the case without the OML, the satellite-derived daily SST was implemented to WRF. The simulated SST looked like a step function that remained unchanged during each hindcast simulation period. Due to heavy cloud coverage, the satellite-derived daily SST data did not resolve the local sea temperature drop during the Hato and Mangkhut crossings. Turning on the OML dynamics, the model did predict a sharp change of SST as Hato and Mangkhut traversed the northern shelf of the SCS.

For Hato, the simulated SST coincided reasonably with the

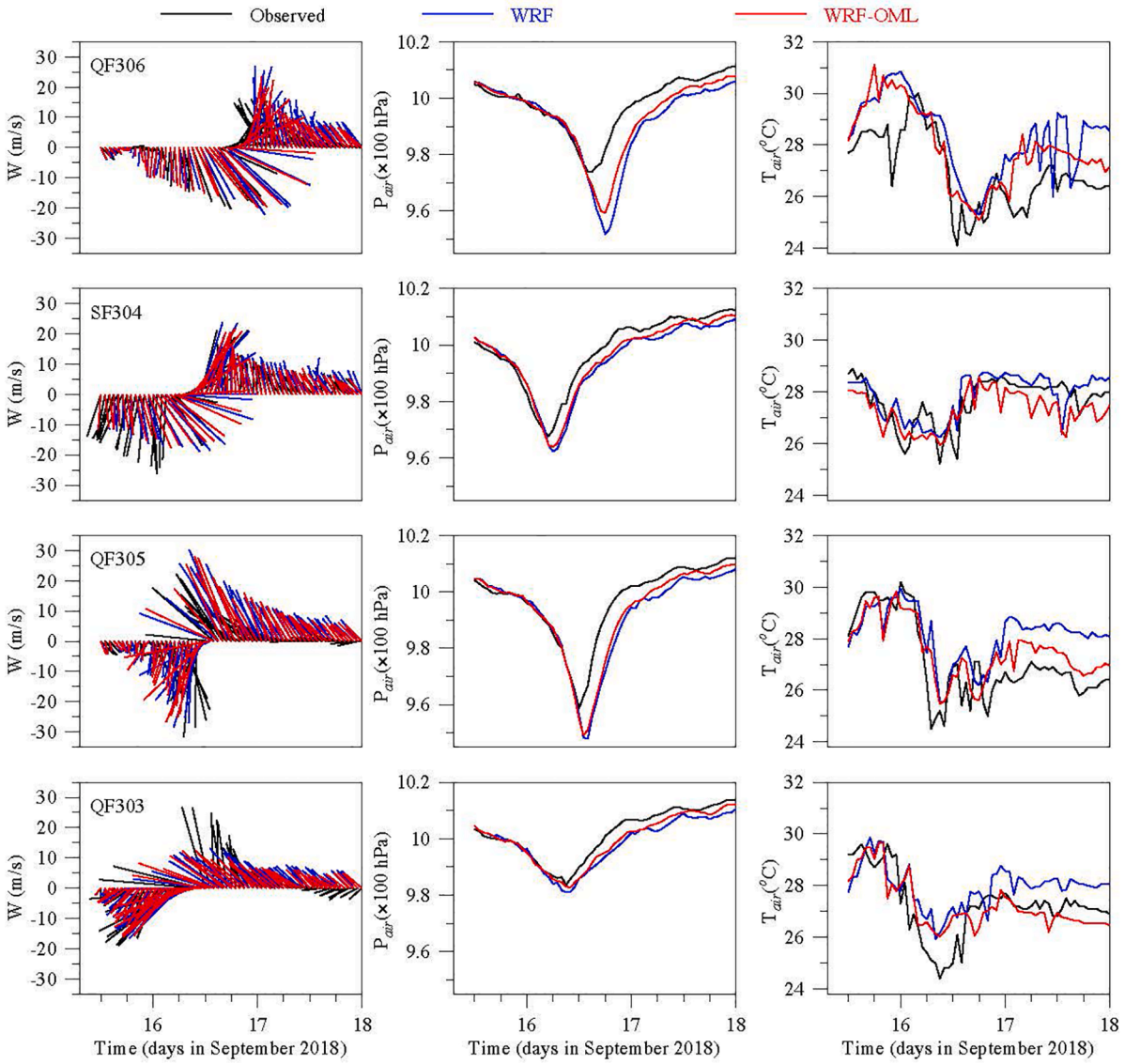

Fig. 10. Comparison between observed and simulated wind vectors (W), air pressures (P_{air}), and air temperatures (T_{air})at QF306, SF304, QF305, and QF303 over September 15–18, 2018, respectively. Black: observed; blue: WRF (without the OML); red: WRF-OML (with the OML). (For interpretation of the references to color in this figure legend, the reader is referred to the web version of this article.)

observation over the period before the typhoon arrived. The timing of the sharp drop of simulated SST also matched that of the observed SST. However, the model significantly under-predicted the magnitude of the SST change. The observed SST showed a drop from 30.1 °C to 26.4 °C, cooling the sea surface by 3.7 °C over 4 h, while the simulated SST only decreased by 1.7 °C, 2.0 °C less than the observation. The simulated OML depth was about 5.0 m on August 22 and rapidly deepened to 26.8 m over a few hours on August 23. Owing to an underestimate in SST, the model seemed to under-predicted vertical mixing in this case.

For Mangkhut, the temporal variation of the simulated SST coincided reasonably with the change of the OML. The simulated OML remained a 2.5-m thickness before 16:00 September 15, which caused the simulated SST to increase by 2.0 °C. The OML rapidly deepened to ~45.8 m over the subsequent 24-hour period, which caused a drop of the simulated SST from ~30.0° to 24.7 °C. The temporal variation of the simulated SST did not agree with the observation. The observed SST first remained unchanged on September 15 and then underwent a significant drop of ~3.0 °C over a subsequent 14-hour period starting at 00:00 September 16. After the passage of Mangkhut, the observed SST experienced a rising period, which was not resolved by the model. It seemed that the model over-predicted vertical mixing in this case.

We compared the simulated and observed latent heat fluxes at buoy sites, and examples were given at QF305 for Hato and QF303 for Mangkhut in Fig. 13. The temporal variations of both observed and simulated latent heat fluxes had the likelihood of relationships with the wind intensity and duration. For Hato, the temporal variations of the simulated wind speed for both the cases with and without the OML reasonably matched with the observations. The main difference was in the magnitude. The simulated maximum winds for the cases with and without the OML were 14.2 and 6.9 m/s weaker than the observations, respectively. After the passage of Hato, the simulated winds were about 2.0–5.0 m/s stronger than the observation. Correspondingly, the observed latent heat flux loss was approximately around zero before Hato arrived, increased to 481.5 W/m^2 as the wind was intensified over the subsequent 13-hour period during the Hato crossing, and then returned to the pre-storm condition over 4 h as the wind rapidly decreased after the passage of Hato. The simulated latent heat fluxes for both the cases with and without the OML agreed with the observation

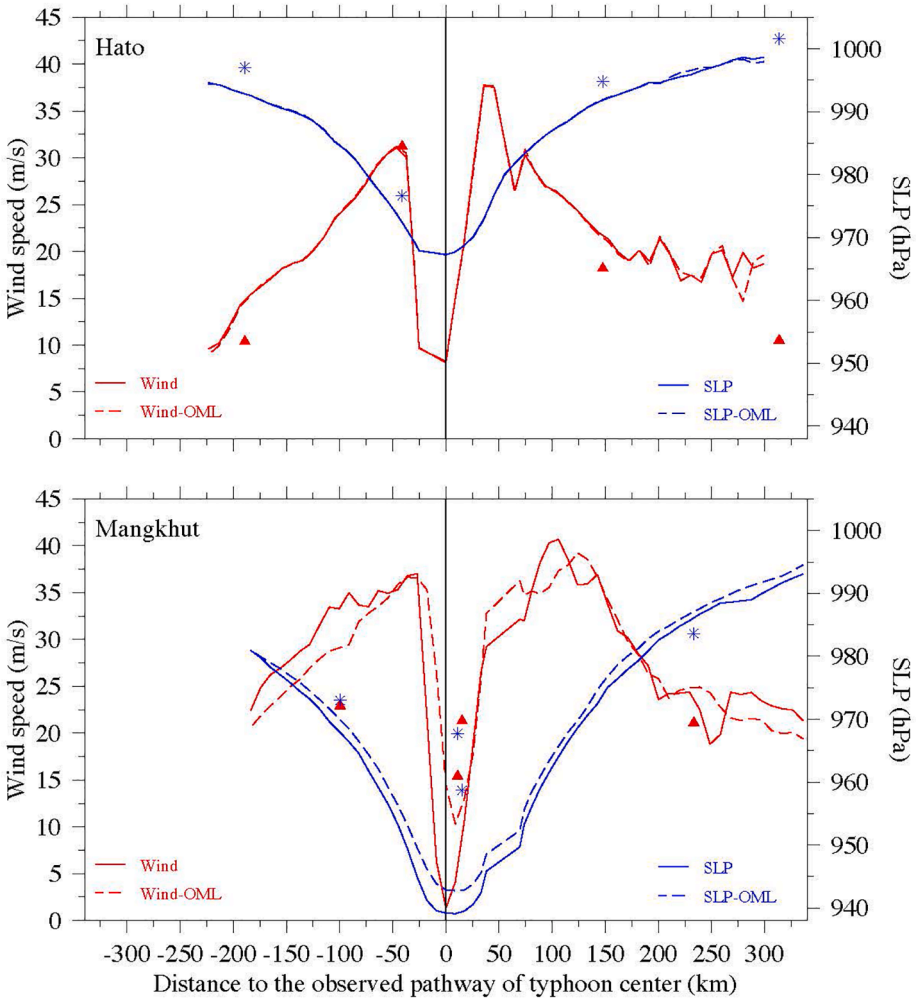

Fig. 11. Distribution of simulated winds (red) and sea level pressures (blue) relative to the typhoon center on the line connecting QF307, QF308, QF305, and QF306 at 08:00 August 23, 2017, for Hato (upper panel) and on the line connecting QF303, QF305, and QF306 at 17:00 September 16, 2019, for Mangkhut (lower panel). The solid and dashed curves refer to the case without and with the OML, respectively. SLP: Sea level pressure. Red filled triangle: the observed wind speed. Blue asterisk: the observed SLP. (For interpretation of the references to color in this figure legend, the reader is referred to the web version of this article.)

before the Hato arrival. However, they underestimated the maximum heat loss from the ocean to Hato during the Hato crossing. The simulated maximum heat loss occurred about ~3 h later than the observation. After the passage of Hato, the observation showed that the ocean turned rapidly from heat-loss to heat-gain, while the simulated latent flux remained under a loss condition.

For Mangkhut, the simulated and observed wind speeds were in reasonable agreement, with the maximum wind speed differences of 0.7 and 2.1 m/s for the cases with and without the OML, respectively. Correspondingly, the simulated latent heat flux agreed reasonably well with the observations throughout rapid wind intensification during the Mangkhut crossing. A significant deviation, however, occurred hereafter. The observed latent heat flux turned back to an oceanic gain condition within one hour after the passage of Mangkhut. In contrast, the simulated latent heat flux remained under an oceanic loss condition for a subsequent day. Including the OML did not show a significant change of latent heat flux, except for a slight enhancement of the oceanic heat loss during the Mangkhut crossing. This result was consistent with the simulated SST, which failed to reproduce surface warming after the passage of Mangkhut.

We also compared the cross-typhoon distributions of observed and simulated daily accumulated latent heats for Hato and Mangkhut. For Hato, although the observed and simulated latent heats displayed the same cross-typhoon distribution pattern, the model significantly overestimated the oceanic heat energy to Hato, with amounts of 22.3% and 197.4% within and outside of the radius of maximum wind. Similarly, for Mangkhut, the model captured the cross-typhoon distribution of the oceanic latent heat, but the model-data difference remained in the same range as that found in Hato.

The latent flux is caused by evaporation. For both model and observation, it was estimated through a product of Monin-Obukhov similarity scaling parameters of the moist air density (ρ_a), the latent heat rate of evaporation of water (L_e), friction velocity (u_*), and water vapor mixing ratio (q_*). L_e is the function of SST. The reason why the model was unable to capture the sharp variability of observed latent heat flux is likely related to its failure to reproduce SST and typhoon-induced vertical mixing.

5. Discussions

The observations revealed the significant different oceanic responses to Hato and Mangkhut. During Hato, the SST decreased rapidly with drops of air pressure and air temperature, forming a well-defined cold wake underneath the storm. This cold wake appeared as a result of intense wind-produced vertical mixing and surface cooling-produced convection/overturning. Compared with Hato, the cold wake was not evident in Mangkhut. The SST did not show a significant drop following the rapid decrease of air temperature at most buoys, where the strong wind and air cooling were recorded. We did observe the remarkable SST drop at Buoy 303, but it was in the marginal zone of storm-induced winds at a distance of ~233 km away from the storm center.

The WRF underestimated and overestimated the minimum sea-level pressure of Hato and Mangkhut, respectively. The sea-level pressure of a storm is a function of air temperature, inverse perturbation density, air moisture, and water vapor mixing ratio. For Hato, the maximum drop of air temperature at QF305 was ~8.0 °C during the Hato crossing.

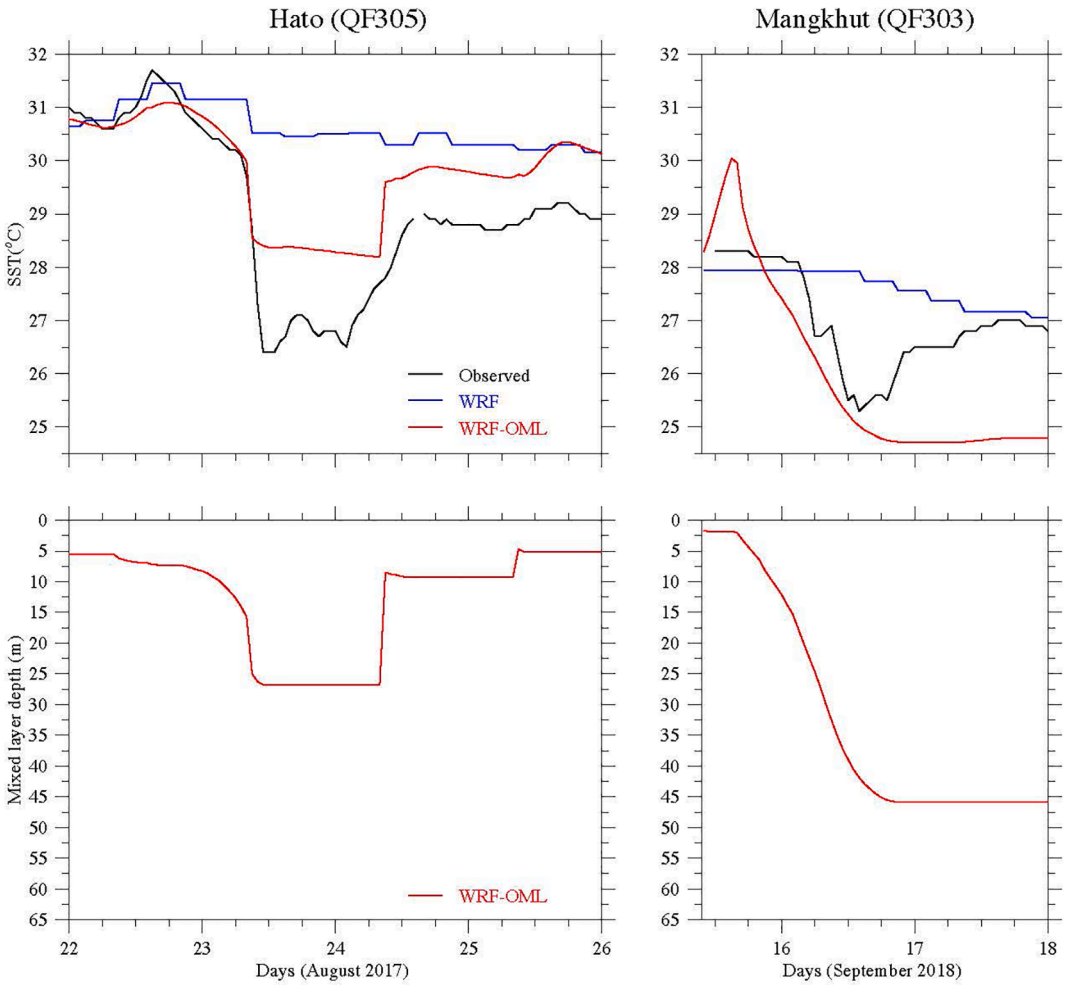

Fig. 12. Upper panels: comparison of the observed SST with the WRF-simulated SSTs in the cases with and without the OML at QF305 over August 22–26, 2017, for Hato (left) and at QF303 over September 15–18, 2018, for Mangkhut (right). Black: observed; blue: WRF (without the OML); red: WRF-OML (with the OML). Lower panels: WRF-simulated depths of the oceanic mixed layer over the same periods for Hato (left) and Mangkhut (right). (For interpretation of the references to color in this figure legend, the reader is referred to the web version of this article.)

Considering only the change of air pressure due to air temperature, we used an empirical formulation of air pressure to estimate an order of magnitude change of air pressure, which was only about 1.8% for an 8.0 °C air temperature drop (Li et al., 2020a). It implied that the underestimate of the simulated air pressure was owing to other parameters relating to air moisture and water vapor mixing ratio, i.e., the storm-enhanced oceanic latent flux loss through the air-sea interface. Since the latent heat flux loss was directly related to storm-induced oceanic mixing, getting oceanic vertical mixing correct in WRF is imperative if one attempts to improve the typhoon simulation.

The convection/overturning is a non-hydrostatic process, which requires an oceanic model to include non-hydrostatic dynamics. The SST recorded on buoys clearly showed that the water was mixed rapidly within a short-time period, which was likely a convection/overturning-dominant mixing feature. Understanding the nature of typhoon-induced oceanic mixing could provide insights into the dynamics of mixing requiring for the ocean and atmospheric coupling.

We have selected PWP and MY2.5 models to assess the importance of convection/overturning to storm-induced oceanic mixing. As we discussed in Section 2, although both PWP and MY2.5 are unable to capture the non-hydrostatic convection process, PWP can directly resolve rapid mixing due to surface cooling-induced overturning, while MY2.5 produces mixing through vertical diffusion over a diffusive time scale. Experiments were made at QF305 for Hato and QF303 for Mangkhut, with initial vertical profiles of temperature and salinity specified using the CTD data (see Section 2).

For Hato (Fig. 14: left panel), both PWP and MY2.5 reasonably reproduced the rapid drop of SST at QF305 during its passage. Intense mixing coincided with the increase of surface wind stress and cooling, representing the shear and buoyancy-induced turbulence productions. PWP and MY2.5 over- and under-estimated the minimum SST, respectively. Considering the period during which SST decreased from 30 °C to the minimum, the observed SST dropped at a rate of ~1.0 °C/h. The simulated SST was reduced by ~1.1 °C/h for PWP and 0.4 °C/h for MY2.5. For MY2.5, if considering only the period with an SST drop from 30 °C to 28 °C, it showed a decrease of ~0.6 °C/h, which was still about 40% lower than the observed SST decrease rate. It suggested that in this case, the rapid SST drop was likely due to cooling-induced overturning, which was reasonably captured by PWP but not by MY2.5.

Both PWP and MY2.5 showed a similar performance over the warming period after the passage of Hato. If shifting the PWP-simulated minimum SST to the same level as the MY2.5-simulated minimum SST, both SST matched each other during the subsequent period with positive net heat flux.

For Mangkhut (Fig. 14: right panel), at QF303, the wind was relatively weak but with a longer duration. Significant surface cooling lasted for about 20 h, almost twice as long as found at QF305 during Hato. It implied that cooling-induced overturning was much more vigorous

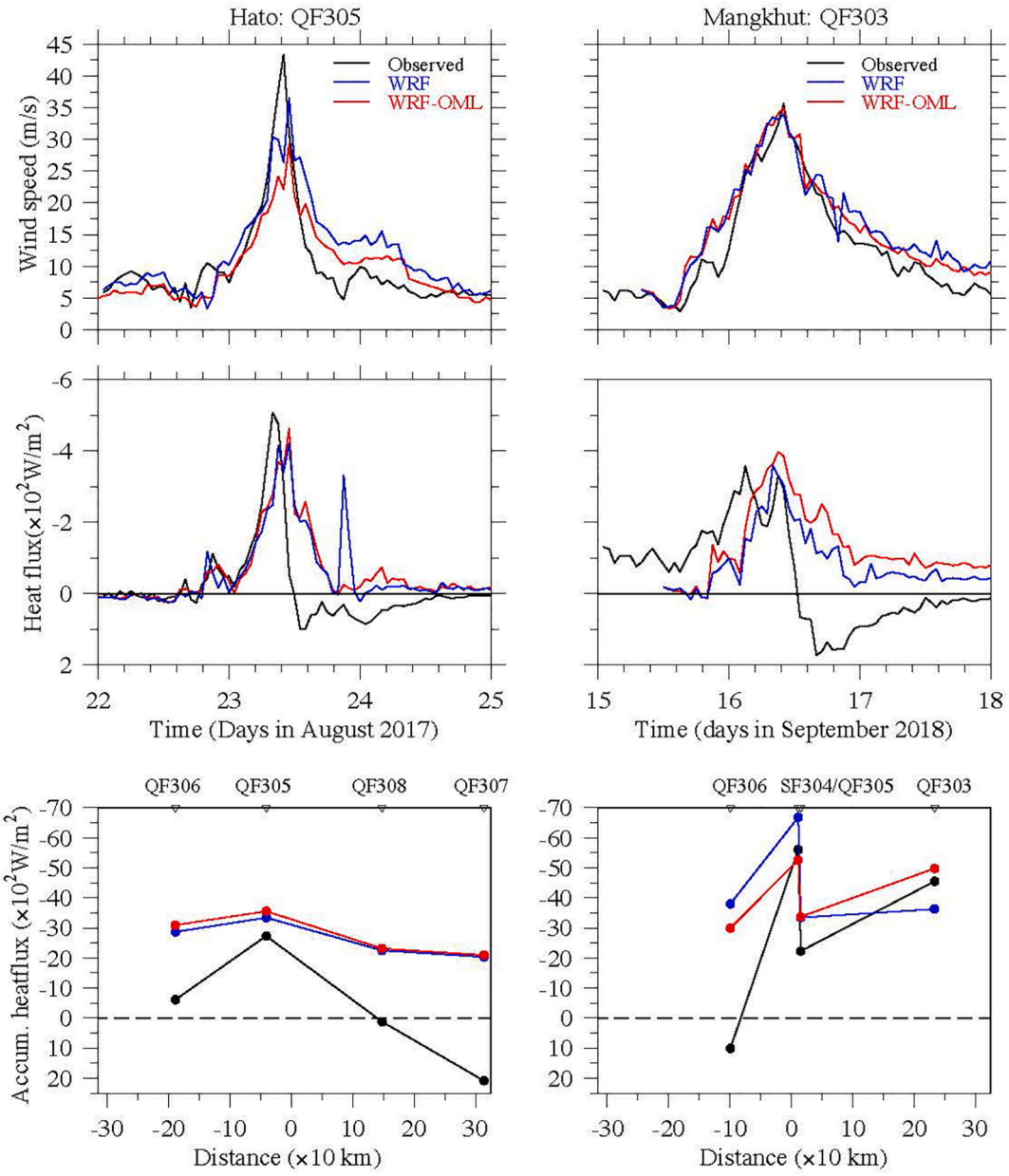

Fig. 13. Upper and middle panels: comparisons between observed and simulated wind speeds and latent heat fluxes over August 22–25, 2017, for Hato (left) and September 15–18, 2018, for Mangkhut (right). Lower panels: comparisons between observed and simulated accumulated daily latent heats for Hato (left) and Mangkhut (right). Black: observed; blue: WRF (without the OML); red: WRF-OML (with the OML). (For interpretation of the references to color in this figure legend, the reader is referred to the web version of this article.)

compared with the Hato case. That was evident from the PWP and MY2.5 simulation results. The PWP-simulated SST agreed with the observed SST during the cooling period, but MY2.5 didn't. The difference in performances of PWP and MY2.5 for this case suggested if cooling-induced overturning dominated mixing, a diffusion-based turbulence closure model could significantly underestimate mixing intensity and timing. This result is consistent with observational findings, which showed that convection/overturning became critically important as the surface cooling duration lasted longer.

It should be noted that PWP failed to capture the surface warming after the passage of Mangkhut, even that the net heat flux remained positive during that period. It seemed that PWP caused an overestimate of the wind stress-produced shear turbulence production during the weak wind zone, which tended to cancel the heating-enhanced vertical stratification. We believe that rapid warming at buoy sites was a result of the post-storm current adjustment process. The storm wind produced a cyclonic oceanic flow. This flow had positive vorticity, which pushed the warmer surrounding water to the storm-influenced area.

We also compared the PWP and MY2.5-produced OML depths at QF305 for Hato (Fig. 15) and QF303 for Mangkhut (Fig. 16). For Hato, PWP showed that the OML depth remained around 5–7 m before Hato arrived, rapidly deepened to ~40 m (bottom) over a few hours during the Hato crossing, and then rose to ~10 m over the warming period after Hato passed. Before Hato arrived, the OML depth changed with both temperature and salinity. After Hato passed, the OML depth only changed with temperature since the salinity remained vertically well mixed. The MY2.5-produced OML depth remained around 5–10 m before Hato arrived, rapidly deepened to ~25 m over a few hours during the Hato crossing, and then gradually rose to ~5 m after Hato passed. The MY2.5-produced maximum OML depth was about 15 m shallower compared with the PWP result. In this case, both temperature and salinity could not be vertically mixed throughout the water column.

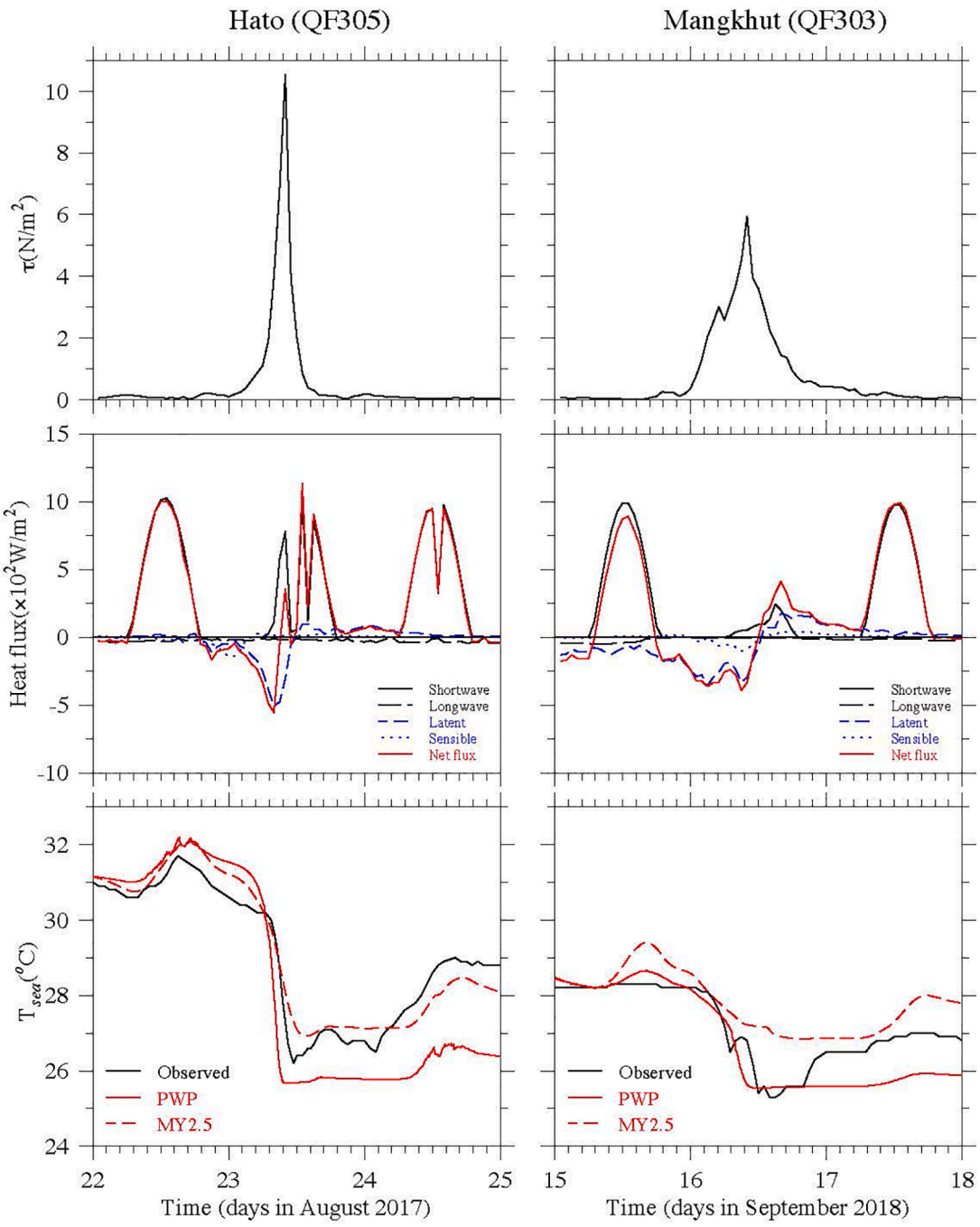

Fig. 14. Upper panels: observed wind stresses at QF305 over August 22–25, 2017, for Hato (left) and QF303 over September 15–18, 2018, for Mangkhut (right). Middle panels: shortwave radiation, longwave radiation, latent heat flux, sensible heat flux, and net heat flux over the same periods for Hato (left) and Mangkhut (right). The definitions for each curve are given inside the figure. Lower panels: comparisons between observed and simulated SSTs over the same periods for Hato (left) and Mangkhut (right). Black: observed; red: PWP-simulated; red dashed: MY2.5-simulated. (For interpretation of the references to color in this figure legend, the reader is referred to the web version of this article.)

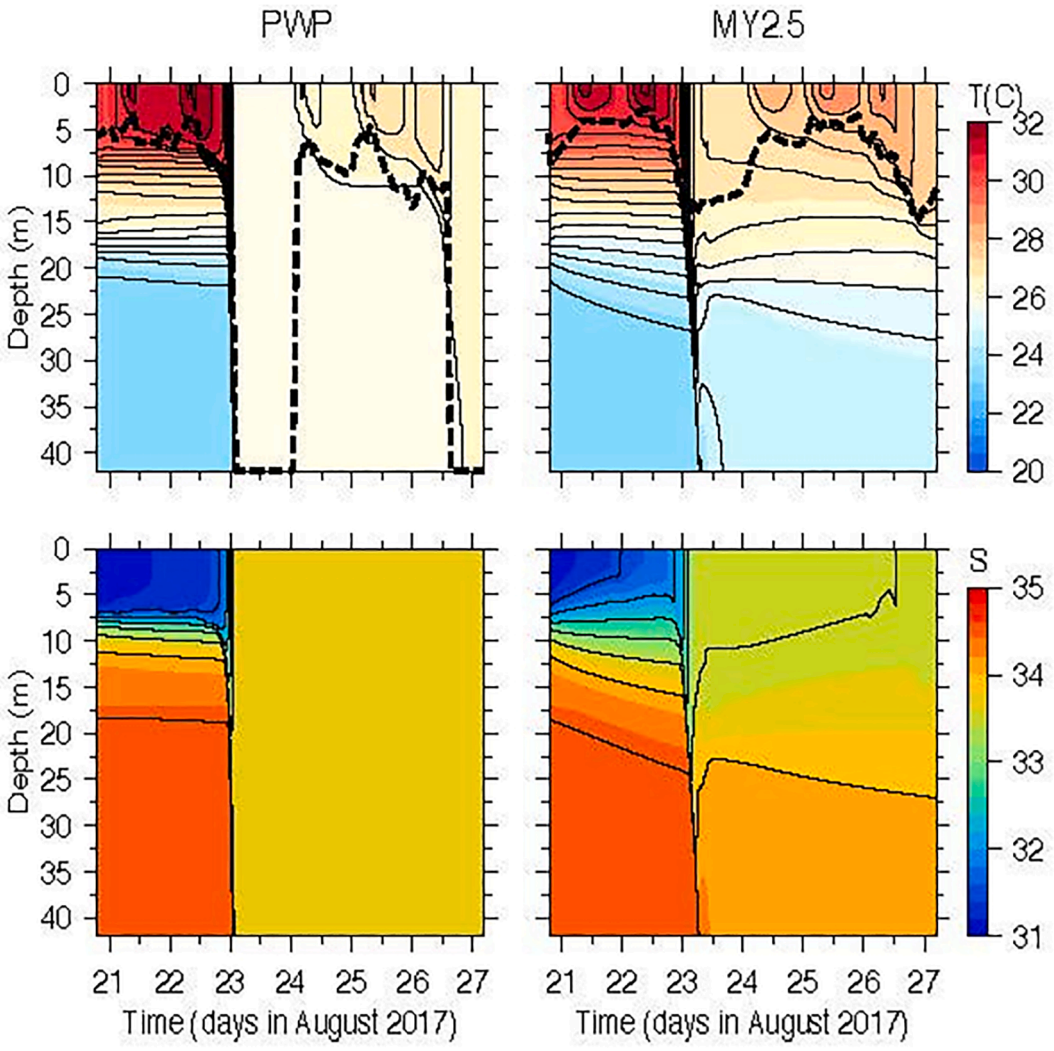

Fig. 15. Temporal variation of the simulated OML depth (thick black dashed line) overlapped with the time series distribution of sea temperature (*T*) and salinity (*S*) over August 21–27, 2017, for Hato. Left panels: PWP-simulated; right panels: MY2.5-simulated.

For Mangkhut, the PWP-produced OML depth remained ~25 m before Mangkhut arrived and then rapidly deepened to the bottom over a few hours during the Mangkhut crossing. As described above, the PWP overestimated the wind stress-produced turbulence mixing over the weakly wind period, so that the OML depth remained unchanged after Mangkhut passed. The MY2.5-produced OML depth remained around 20.0–25.0 m before Mangkhut arrived, deepened to ~35.0 m over 8 h during the Mangkhut crossing, and then gradually rose to ~20.0 m over the subsequent day after Mangkhut passed. The maximum OML depth was about 25.0 m shallower in the MY2.5 than in the PWP. MY2.5 reproduced the surface warming after Mangkhut passed.

We also compared PWP and MY2.5-produced maximum OML depths with the WRF result for the case with the OML. For Hato, the WRF-produced maximum OML depth was close to the MY2.5 result but significantly shallower than the PWP result. For Mangkhut, the WRF-produced maximum OML depth was close to the PWP result. However, before Mangkhut arrived, the WRF-produced OML depth was too shallow compared with the PWP and MY2.5 results.

Our interests are to examine whether the diffusion-based turbulence closure model can capture cooling-induced rapid mixing during storms, with no intention to compare the performance of PWP and MY2.5 OML models for storm-induced mixing. Our results suggest that MY2.5 did not

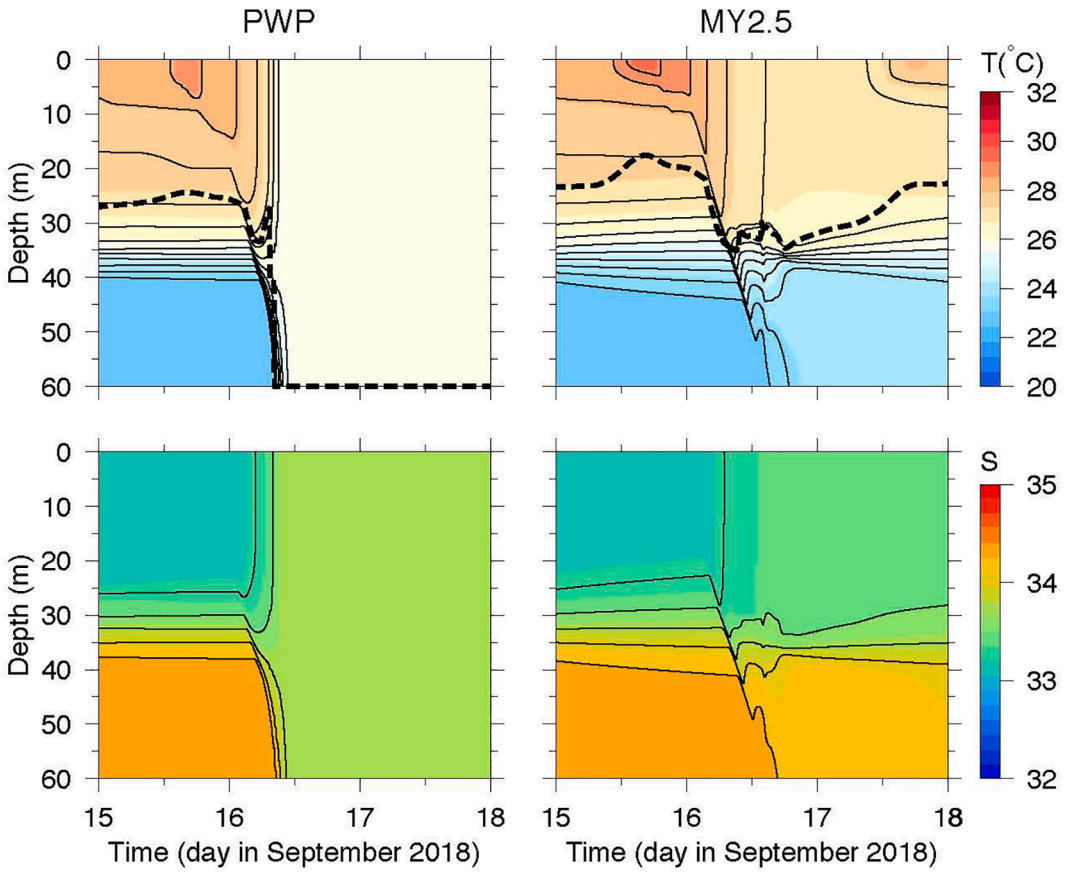

Fig. 16. Temporal variation of the simulated OML depth (thick black dashed line) overlapped with the time series distribution of sea temperature (*T*) and salinity (*S*) over September 15–18, 2018, for Mangkhut. Left panels: PWP-simulated; right panels: MY2.5-simulated.

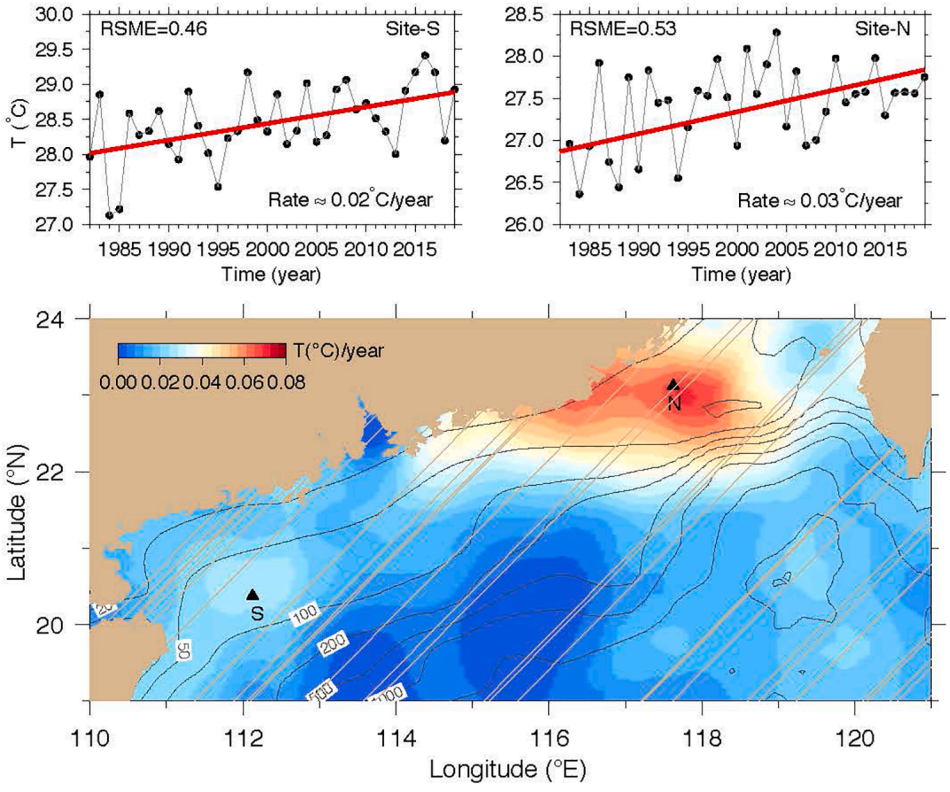

Fig. 17. Lower panel: distribution of the yearly summertime temperature increase rate calculated based on the satellite-derived SST data over 1982–2019. The temperature increase rate was estimated based on the annual increase rate calculating over two consecutive years. Upper panels: the change of the satellite-derived summertime SST at site S (left) and site N (right) over 1982–2019. Solid black dots: the summertime averaged SST for each year; thick red line: the linear regression fitting line. (For interpretation of the references to color in this figure legend, the reader is referred to the web version of this article.)

capture the cooling-induced rapid mixing rate, even though it did provide a good SST simulation in the Hato case. It implies that a coupled atmospheric-ocean model might not capture storm-induced rapid oceanic mixing and heat energy transfer process if mixing in the ocean component of this model is parametrized through a diffusion-based turbulent closure model. Since storm-induced rapid mixing is mainly caused by surface cooling, it is critical to improving the physics of vertical mixing, particularly to include the non-hydrostatic convection/overturning process.

Stratification in the ocean varies with both temperature and salinity. Over the northern shelf of the SCS, the salinity has an equivalent contribution as the temperature to vertical stratification. The purely temperature-dependent OML model in WRF should also be improved by including salinity.

The comparison results of in-situ and climatological T/S profiles (Fig. 6) indicated that the water over the northern shelf of the SCS was much fresher and warmer in recent years. We collected the satellite-derived SST data over the period 1982–2019 and calculated the yearly change rate of the SST in the summer season (Fig. 17). The results show that the northern shelf of the SCS is warming, at a yearly temperature increase rate varying significantly in space. For example, at sites N and S, the SST changed interannually with an oscillation period of ~2–3 years and fluctuated considerably with an amplitude up to ~2 °C. The yearly linearly-fitting warming rates at these two sites were 0.03 °C/year and 0.02 °C/year, respectively. The distribution of the warming rate shown in the lower panel of Fig. 17 was calculated using the average annual increase rate over two consecutive years, which were higher than the least-square linearly-fitting result shown in the upper panel.

The warming tendency over the northern shelf of the SCS has significantly intensified the water stratification and made the OML shallower in the summer season. As a result, the air-sea interaction could be more energetic for typhoons through storm-induced oceanic mixing. It was evident in Hato during which the OML depth was only 5-m before the storm. Although our interests in this paper were on the short-term oceanic responses to typhoons, the future WRF simulation should consider warming effects on TCs.

We also want to clarify here that the experiments with the OML were made using the 1-D OML models. Yablonsky and Ginis (2009) pointed out that coupling a 1-D ocean model with a 3-D hurricane model could significantly underestimate the storm-core sea surface cooling. Li et al. (2020) compared the results of the WRF with and without the 1-D OML model for the Hurricane Sandy simulation. They found that the 1-D OML was robust to capture the storm-induced cold wake and significantly improved the storm's intensity and trajectories. Further efforts should be made to verify the criterion needed for a 3-D OML model in real-time storm simulations.

6. Conclusions

A storm-monitoring system consisting of 8 meteorological buoys were established over the northern shelf of the SCS. This system captured the changes of meteorological and oceanic conditions during Hato in August 2017 and Mangkhut in September 2018. The observations showed that with similar shelf-traversing trajectories, these two typhoons significantly differed in storm-induced oceanic mixing, oceanic heat transfer through the air-sea interface, and surface waves. Storm-induced vertical mixing caused a rapid sea temperature drop during the Hato crossing but not during the Mangkhut crossing. As a result, a well-defined cold wake formed underneath Hato but not Mangkhut. Impacts of oceanic mixing on forming a storm-produced cold wake were associated with the pre-storm conditions of water stratification and depth of the OML. In addition to oceanic mixing produced by shear turbulence production, cooling-induced overturning was a physical process that led to rapid mixing in the OML. This process played a more important role in mixing if the atmospheric cooling duration above the sea surface lasted longer.

Storm-generated maximum latent flux was generally 3 or 4 times greater than the maximum sensible flux. The transfer of oceanic latent heat flux to typhoon varied with wind intensity and duration. Behaviors of storm-generated surface waves exhibited a distinct difference for storms under the different development status (Appendix C). For an intensified typhoon (Hato), the windsea waves with shorter peak periods were dominant, while for a weakened typhoon (Mangkhut), swell waves with longer peak periods could be as strong as windsea waves.

The WRF model captured the storm-induced variations of wind and sea-level pressure but not air and sea temperatures. Turning on the OML in the WRF simulation resolved the storm mixing-induced SST drop. However, the OML model in WRF significantly underestimated the maximum decrease of SST and failed to resolve the sharp variation of storm-enhanced latent heat flux. It was one of the reasons why the simulated oceanic feedback to air pressure and winds was insignificant.

Process-oriented OML model experiments supported the observational finding: rapid mixing was mainly caused by surface cooling-induced overturning. For Hato, the change of surface wind stress and cooling occurred within a short-time period. In this case, both diffusion-based and bulk shear instability OML models enabled to capture the observed SST drop, even though the diffusion-based OML model significantly underestimated the observed rapid mixing rate. For Mangkhut, since the surface air cooling lasted for a more extended period, storm-induced mixing was dominated by the cooling-induced overturning process, which was well captured by a bulk instability OML model but not by a diffusion-based OML model. To simulate the realistic OML and vertical mixing, a coupled atmosphere–ocean model needs to improve the physics of vertical mixing with non-hydrostatic convection/overturning.

Both observations and model experiment results show that the importance of the typhoon-induced air-sea interaction is related to water stratification and the OML depth. Climate-induced warming tends to intensify the water stratification and shallow the OML over the northern shelf of the SCS, projecting a more energetic influence on typhoon intensity and pathway in the future.

Declaration of Competing Interest

The authors declare that they have no known competing financial interests or personal relationships that could have appeared to influence the work reported in this paper.

Acknowledgments

This work was supported by the National Key Research and Development Programs of China with grant numbers 2018YFC-1406201; 2016YFA-0602700; 2018YFC-1506903; 2018YFC-1406205, and the National Sciences Foundation of China with grant number U1811464. S. Li was supported by the oversea Ph.D. fellowship from the China Scholarship Council (No. 1409010025) and Dr. Chen's Montgomery Charter Chair graduate education funds at the University of Massachusetts-Dartmouth.

Appendix A. Time series recorded at individual buoy sites

Time series of wind vector, air pressure, oceanic current vector, significant wave height, air temperature, and sea temperature at buoys, including QF306, QF307, QF308, and SF301 for Hato and QF304, QF305, QF306, SF306, and QF304 for Mangkhut (Fig. 2), were shown in Figs. A1–A3. QF304,

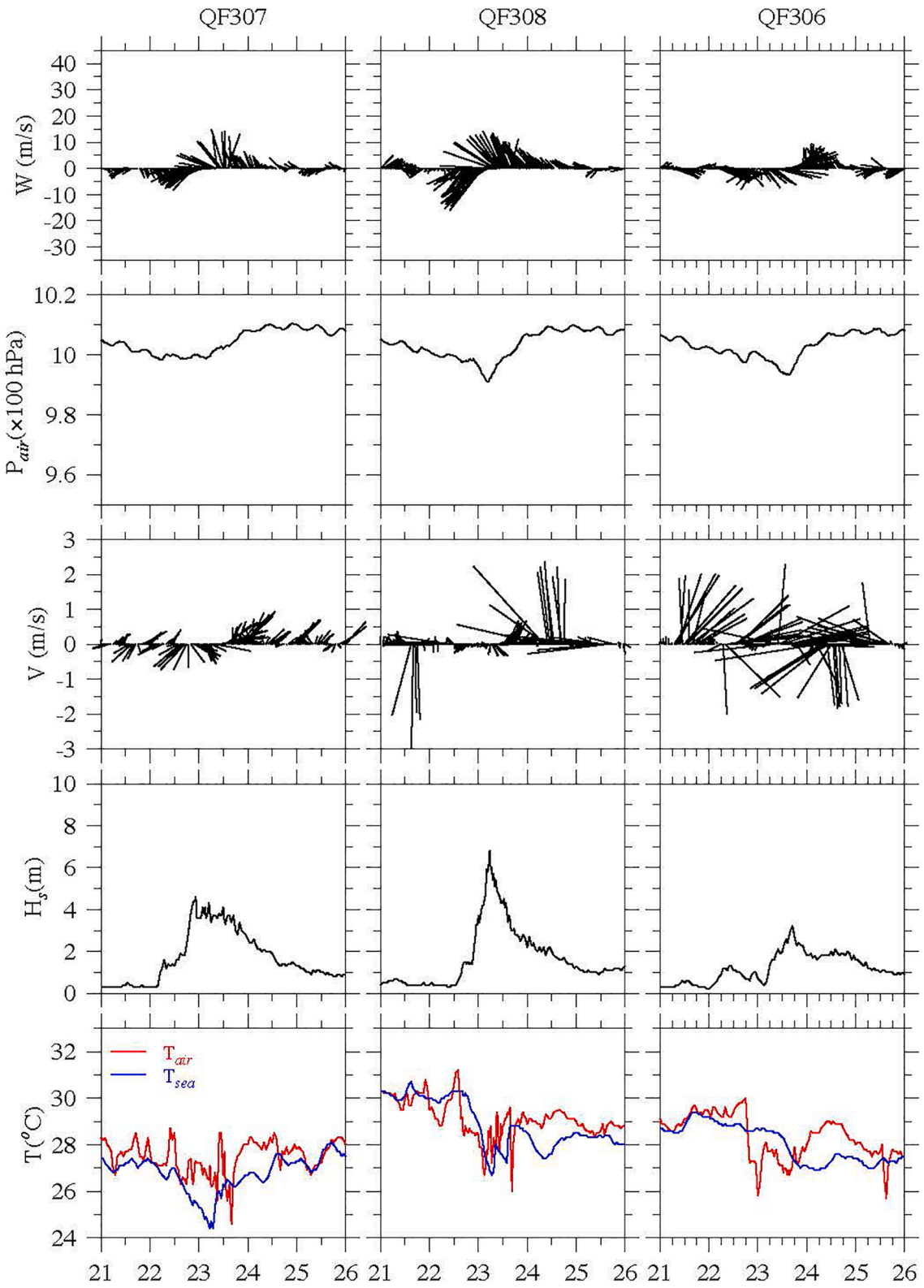

Fig. A1. Time series of wind vector (W), air pressure (P_{air}) oceanic current vector (V), significant wave height (H_s), air temperature (T_{air})and sea temperature (T_{sea}) recorded at QF306, QF307, and QF308 during the Hato crossing over August 21–26, 2017, respectively.

QF305, QF306, QF307, and QF308 were located along the 50-m isobath, SF301 and SF306 were over the slope around 1500–2000-m isobaths, and QF304 was in the Gulf of Tonkin, SCS.

A.1. Cross-center structure of Hato

In addition to the description given in Figs. 5 and 7, the cross-center features of Hato can also be viewed with detail at QF306, QF307, and QF308 (Fig. A1). The wind intensity decreased rapidly with the Hato center's distance, with the maximum speeds of 20.7 m/s and 15.7 m/s at QF308 and QF307 on the right and 19.1 m/s at QF306 on the left. The wind weakened by 55% over a 47.9-km distance between QF306 and QF305. The air pressure exhibited a similar distribution, with the minimum values of 991.0, 998.3, and 993.3 hPa at QF308, QF307, and BQF306. The surface waves were dominated by the windseas at QF308 but not at QF307 and QF306. At QF308, the maximum significant wave height was 6.8 m, occurring around the maximum wind speed. At QF307, however, the maximum speed occurred at noon on August 23, while the maximum significant wave height was observed at 21:30 August 22, about 14.5 h earlier. It was clear that QF307 prevailed with swell waves propagating from the remote region.

Similarly, at QF306, the maximum significant wave height was 3.2 m, occurring 1.5 h after the maximum wind. It suggested that both windsea and swell waves occurred at this typhoon wind marginal site. The temporal changes of air and sea temperatures at QF308 were very similar to those observed at QF305 but not at the other two buoys. At QF306, the air temperature decreased from 30.0 °C to 25.8 °C over 6 h starting at 18:00 August 22, while over this period, the sea temperature remained unchanged. At this site, the significant sea temperature drop occurred during the rising period of air temperature, being cooled by 1.4 °C over 16 h. At QF307, the air temperature fluctuated considerably with a magnitude of up to 3.9 °C during August 22–23, whereas the sea temperature decreased monotonically over that period.

The oceanic currents near the sea surface were not driven solely by the wind, although the flow turned counterclockwise like a TC at all buoys during Hato's crossing. At QF306, the maximum current velocity exceeded 2.3 m/s, even though the maximum wind speed was about 1.8 times weaker than the maximum wind at QF305. Such the wind intensity remained during a weakly wind period. Similarly, at QF308, a strong southward flow with a magnitude of >2.0 m/s was observed during the weakly wind period. A northwestward or westward flow with the same order of magnitude appeared again over the subsequent period from 08:00 to 12:30 on August 23. During that period, the wind gradually weakened as the air pressure increased. At QF307, the flow and wind were often in opposite directions during the Hato crossing. The theory of the cyclonic wind-driven circulation could not be used to explain this observed feature.

A.2. Cross-center structure of Mangkhut

The additional cross-center features of Mangkhut can be viewed at QF303, QF305, and QF306 (Fig. A2). At all buoys, the wind turned counterclockwise, a typical characteristic of the storm-induced cyclonic wind. The wind speed and direction changed with air pressure, increasing as air pressure decreased, turning ~180° at the time of the minimum air pressure, remaining strong during the rapid increase period of air pressure, and then weakening rapidly after Mangkhut passed. The minimum air pressures were 983.6, 958.7, and 973.0 hPa occurring at 09:30, 12:30, and 14:30 on September 16 at QF303, QF305, and QF306, respectively. The maximum winds during the decrease and increase air pressure periods were 35.6 and 29.9 m/s at QF303; 32.0 and 28.1 m/s at QF305; and 22.9 and 22.5 m/s at QF306, respectively.

Mangkhut-generated surface waves behaved differently from those observed in Hato. At QF305, QF303, and QF306, the observed maximum significant wave heights at these buoys were greater during Mangkhut than during Hato, even though the maximum winds at these buoys were weaker. This evidence suggested that during Mangkhut, the observed surface waves over the northern shelf of the SCS contained a significant component of swell waves.

As the same as Hato, during the Mangkhut crossing, the air temperature dropped significantly as air pressure decreased, with a maximum drop of 5.2 °C at QF303, 5.2 °C at QF305, and 5.6 °C at QF306. However, the near-surface sea temperature did not significantly reduce like the air temperature at all buoys except QF303, even though the strong wind was recorded and also the air was colder than the seawater.

The oceanic flow responses to Mangkhut were not highly related to the wind changes recording on buoys. At QF303, for example, the flow was intensified with the wind speed, but its direction remained southward no matter how the wind direction changed. At QF306, a strong flow was observed during a weakly wind period before Mangkhut arrived.

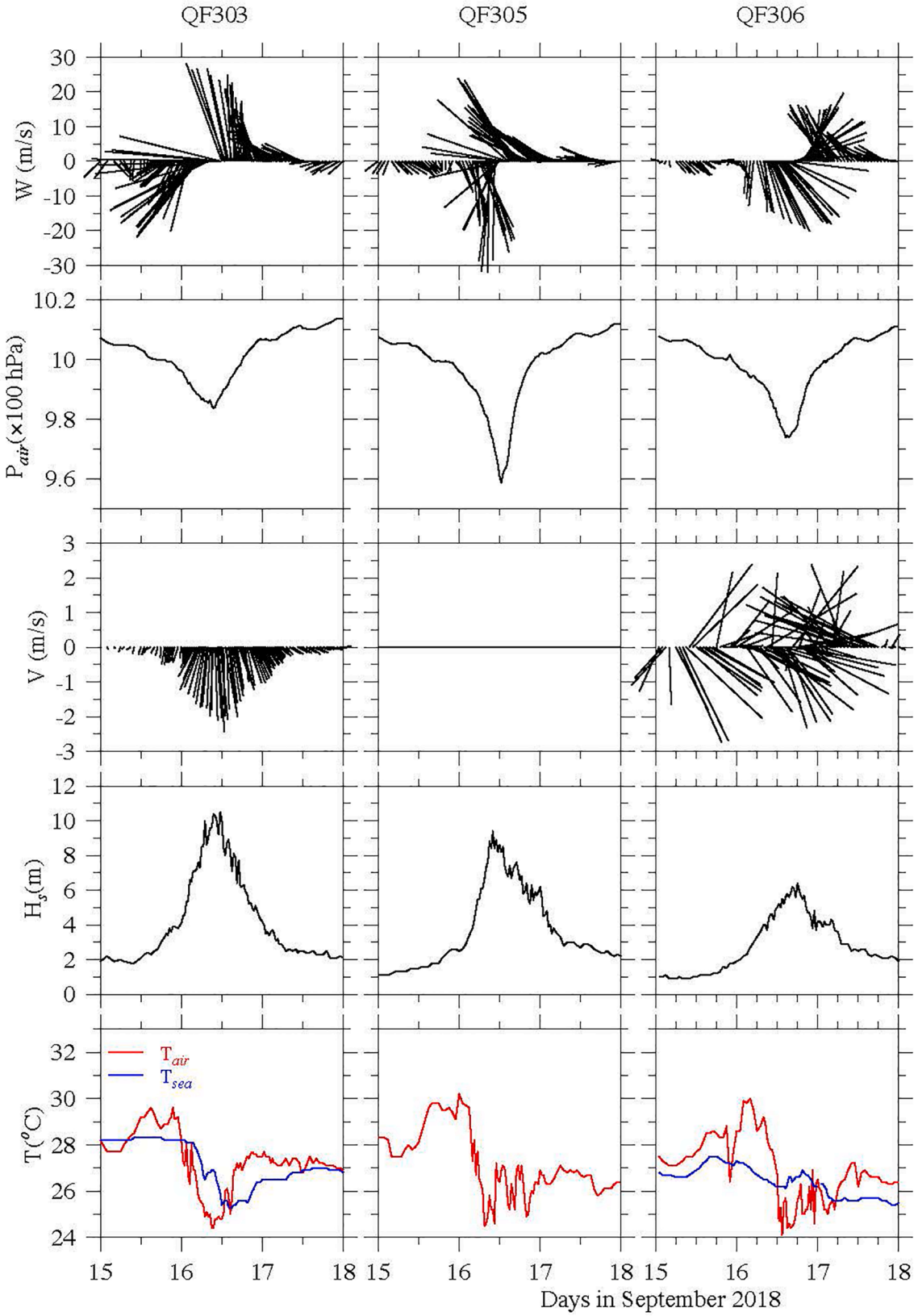

Fig. A2. Time series of wind vector (*W*), air pressure (P_{air}) oceanic current vector (*V*), significant wave height (H_s), air temperature (T_{air})and sea temperature (T_{sea}) recorded at QF303, QF305, and QF306 during the Mangkhut crossing over September 15–18, 2018, respectively.

A.3. Features observed over the slope

SF301 was located on the left side of Hato with the shortest distance of ~148.0 km away from its center. When Hato traversed the slope and moved towards the coast, the air pressure at this buoy dropped by 2.9 hPa during the first 7 h and then increased by 3.0 hPa over the next 8 h. A minimum of 993.0 hPa occurred at 04:00 August 23 (Fig. A3). Correspondingly, the wind rotated counterclockwise, intensifying as air pressure decreased, reaching its maximum of 16.8 m/s around the minimum air pressure, and then gradually weakening as air pressure increased. Two unique features were observed at this buoy. First, the maximum significant wave height was 4.6 m, appearing 6.5 h later than the maximum wind. It was clear that Hato-generated surface waves over the slope contained a large portion of swell waves. Second, the air temperature showed a drop of ~7 °C during the Hato crossing, but the near-surface sea temperature did not show a significant decrease. That completely differed from what happened at buoys over the shelf.

SF306 was located on the left side of Mangkhut with the shortest distance of ~553 km from the storm center. Although this buoy was far away, the

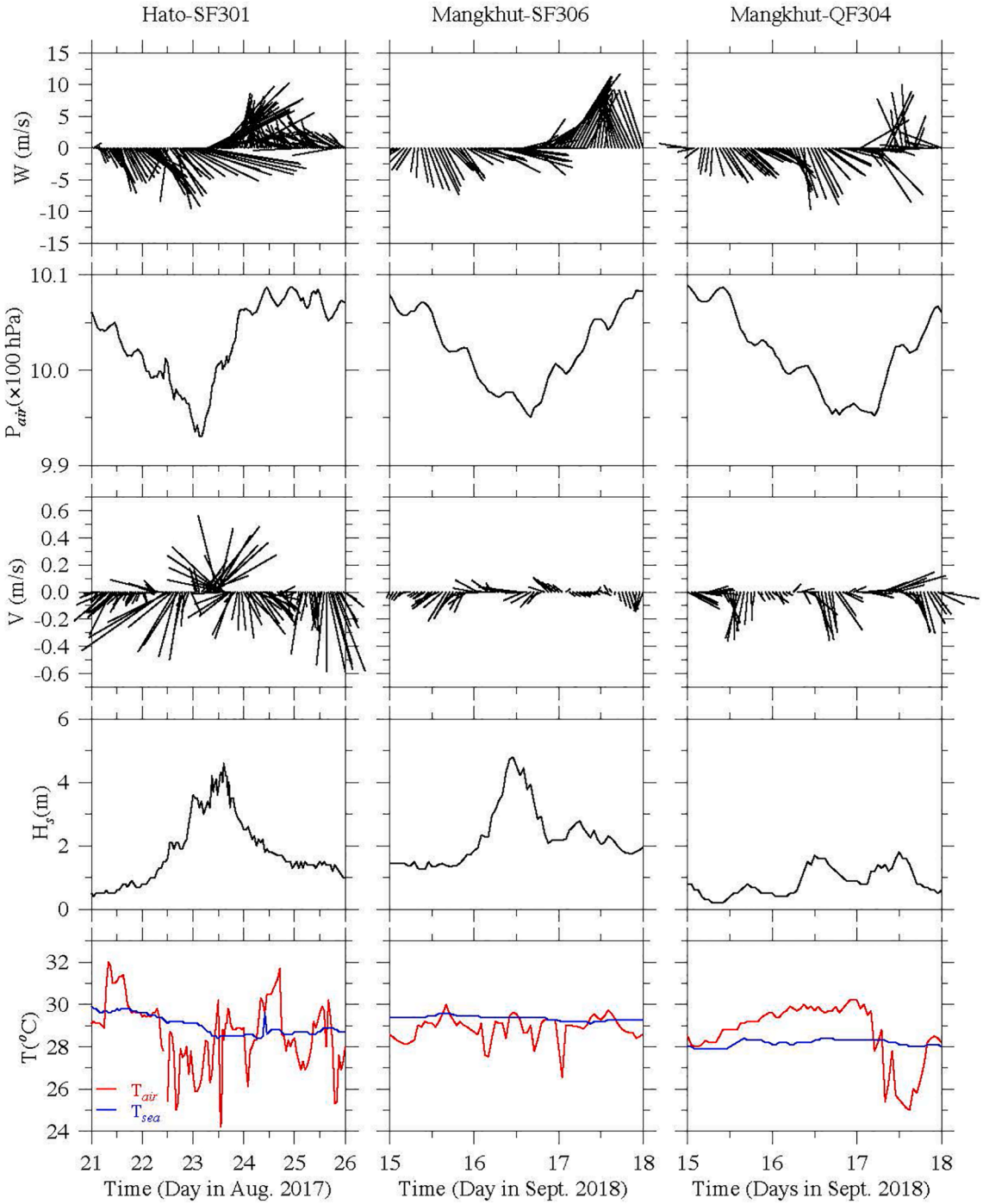

Fig. A3. Time series of wind vector (W), air pressure (P_{air}) oceanic current vector (V), significant wave height (H_s), air temperature (T_{air})and sea temperature (T_{sea}) recorded at SF301 over August 21–26, 2017 and at SF306 and QF304 over September 15–18, 2018, respectively.

storm's influence was evident (Fig. A3). The air pressure dropped by 5.2 hPa, accompanying by intensified, counterclockwise- rotated wind and the appearance of relatively strong surface waves. The maximum wind reached 14.8 m/s, occurring during an increased air pressure period after Mangkhut entered the slope. The maximum significant wave height was 4.8 m, occurring about 13 h before the maximum wind. The peak wave period was 13.0–15.0 secs, which appeared to be swell waves propagating from the deep basin. The near-surface air temperature fluctuated significantly with a magnitude up to ~2.0 °C, but the near-surface sea temperature remained little change. During most time of that period, the air remained warmer than seawater. It was surprising that no strong currents were observed at SF306 during the Mangkhut crossing through the slope.

A.4. Feature observed in the Gulf of Tonkin

QF304 was much far away from Mangkhut's center. Although this buoy was outside the typhoon's significant influence area, the wind and air pressures still exhibited the same influence level as those at SF306 (Fig. A3). No strong surface waves were observed. The maximum significant wave height was only ~1.9 m. The near-surface air temperature experienced a sharp decrease period, with a maximum drop of ~5.0 °C over 13 h after the minimum air pressure appeared. However, the near-surface sea temperature remained almost unchanged. This finding was the same as at the other shelf and slope buoys, suggesting that oceanic feedback to this typhoon was much weak compared with Hato.

Appendix B. Comparisons of Storm-generated surface waves for Hato and Mangkhut

Behaviors of storm-generated surface waves significantly differed for Hato and Mangkhut. Define T_{lag} as the time lag of the maximum wave height relative to the maximum wind, T_{wd} as the duration of the wind greater than 20.0 m/s, andT_{sd} as the duration of surface waves with a significant wave height of ≥5.0 m. For Hato, the significant wave height increased synchronously with the wind speed, with a maximum height coinciding as the strongest wind (Fig. A4).T_{lag} was 0.0, −1.0, 1.0 and 3.0 hrs. at QF307, QF308, QF305, and QF306, respectively, with peak periods in the range of

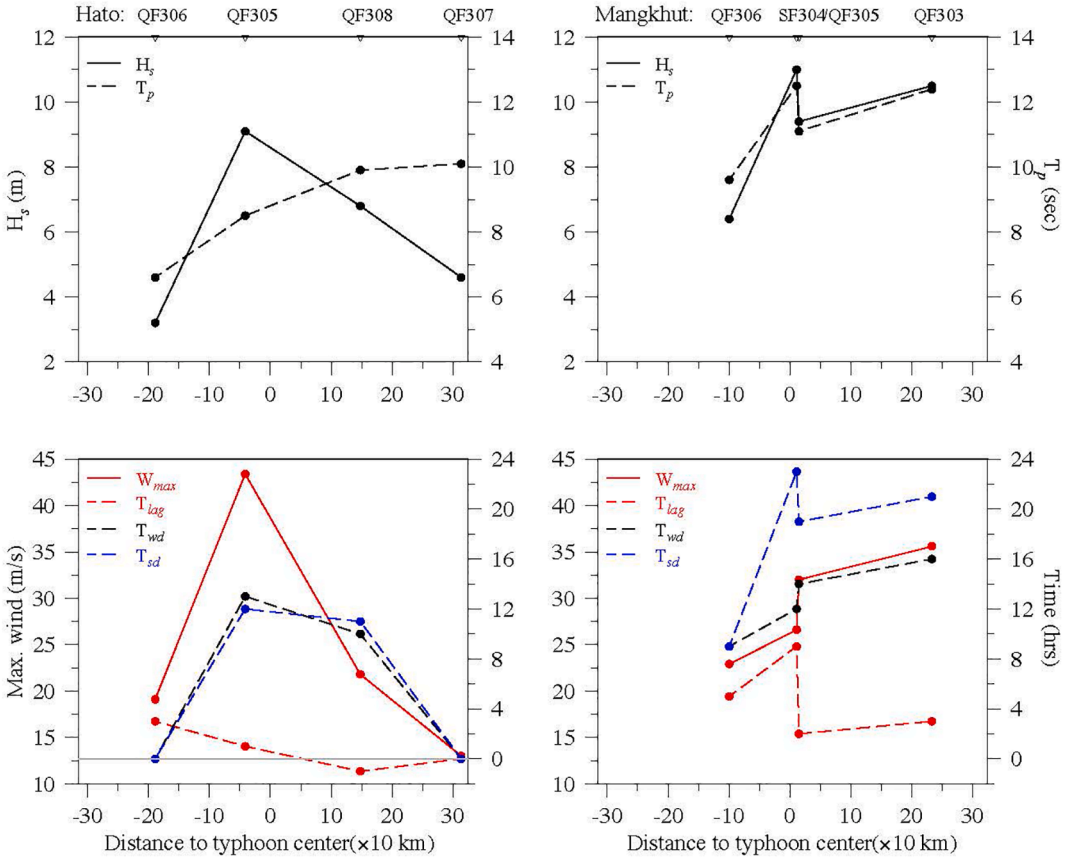

Fig. A4. Cross-typhoon distributions of significant wave height and peak period (upper panels), the lag of the maximum wave height relative to the maximum wind (T_{lag}), the duration of the wind that was ≥20.0 m/s (T_{wd}), the duration of surface waves with a significant wave height of ≥5.0 m (T_{sd}) and the maximum wind speed over T_{wd} (W_{max}) (lower panels) for Hato (left) and Mangkhut (right), respectively.

6.6–10.1 secs. At all these buoys,T_{wd} was directly proportional to T_{sd}, suggesting that during Hato, the windsea waves were dominant (Gilhousen and Hervey, 2001).

For Mangkhut, significant wave height was proportional to the peak period; the higher wave had a more extended period. However, the significant wave height did not increase monotonically with the wind speed. The maximum wave height was observed at QF304, at which the maximum wind speed was weaker than those at AF305 and QF303. T_{lag} was much longer for Mangkhut than for Hato, with a maximum value of 9.0 hrs. at QF304. T_{wd} did not show a proportional relationship with T_{sd}. The longest T_{sd} was observed at QF304, where T_{wd} was much shorter compared with that at either QF305 or QF303. This evidence indicated that Mangkhut-generated surface waves were predominated by both windsea and swell waves, while in the area closed to the typhoon's center, strong swell waves dominated.

Appendix C. Taylor statistics for the model-data comparison

Statistics for the model-data comparison at all buoys were presented using Taylor diagrams shown in Fig. A5, which contained the standard deviation, correlation coefficient, and root square mean error (RSME). For the wind speed, the observed and simulated standard deviations were close to each other for both Hato and Mangkhut, suggesting that the model captured the observed temporal variability. The correlation coefficients with the observed wind were ~0.81 for Hato and ~0.87 for Mangkhut, with RSMEs of <3.0 and ~3.7 m/s, respectively. Including the OML increased the correlation coefficient by ~0.01 for Hato and ~0.03 for Mangkhut, with RSME reductions of ~0.2 and 0.7 m/s, respectively. For the wind direction, both the observed and simulated standard deviations were around 100°, with a high correlation coefficient of >0.92 and an RSME of <40° for both Hato and Mangkhut. For the air pressure, the observed and simulated standard deviations were around 5.0 hPa for Hato, but was ~2.0 hPa larger for Mangkhut. For Hato, including the OML did not significantly improve either correlation coefficient or RMSE. They were >0.92 and around 2.0 hPa regardless of whether the OML was taken into account. For Mangkhut, however, including the OML did show a remarkable improvement in correlation coefficient and RSME. They were <0.90 and ~6.0 hPa for the case without the OML. These two numbers increased to >0.92 and reduced to 4.0 hPa for the case with the OML. For the air temperature, the model underestimated the temporal variability with a difference of 0.2 °C in standard deviation for both Hato and Mangkhut. Including the OML did show a significant improvement for Mangkhut but not for Hato. The correlation coefficients were ~0.35 for Hato and ~0.7 for Mangkhut, with RSMEs of ~1.3 and ~1.2 °C, respectively, no matter whether the OML was considered or not. It was clear that the model provided a better simulation of air temperature for Mangkhut.

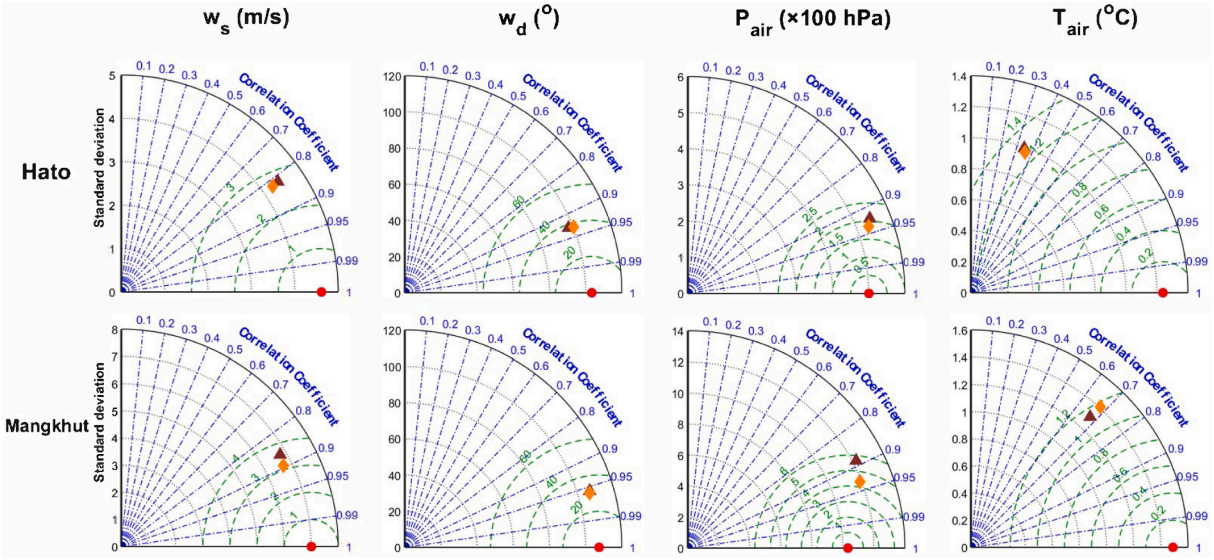

Fig. A5. Taylor diagrams summarizing the comparisons of observed and simulated wind speeds (W_s), wind directions (W_d), air pressures (P_{air}), and air temperatures (T_{air}) for Typhoon Hato (upper panel) and Typhoon Mangkhut (lower panel).

References

Beardsley, R.C., Lentz, S.J., Weller, R.A., Limeburner, R., Irish, J.D., Edson, J.B., 2003. Surface forcing on the southern flank of Georges Bank, February-August 1995. J. Geophys. Res.-Oceans 108, 8007. https://doi.org/10.1029/2002JC001359.

Braun, S.A., Tao, W.K., 2000. Sensitivity of high-resolution simulations of Hurricane Bob (1991) to planetary boundary layer parameterizations. Mon. Weather Rev. 128, 3941–3961. https://doi.org/10.1175/1520-0493(2000)129<3941:SOHRSO>2.0.CO;2.

Burchard, H., 2002. Applied Turbulence Modeling in Marine Waters. Springer, Berlin-Heidelberg-New York-Barcelona-Hong Kong-London-Milan Paris-Tokyo, p. 215.

Chan, J.C., Liu, K.S., Ching, S.E., Lai, E.S.T., 2004. Asymmetric distribution of convection associate with tropical cyclones making landfall along the South China coast. Monthly Weather Rev. 132, 2410–2420.

Chen, D., Lei, X., Wei, W., Wang, G., Han, H., Lei, Z., 2013a. Upper ocean response and feedback mechanisms to typhoon. Adv. Earth Sci. 28 (10), 1077–1086.

Chen, L.S., Yin, Y.H., 1979. An introduction to the Western Pacific Typhoon. China Science Press, Beijing, pp. 91–157 (in Chinese).

Chen, C., Beardsley, R.C., Cowles, G., Qi, J., Lai, Z., Gao, G., Stuebe, D., Liu, H., Xu, Q., Xue, P., Ge, J., Ji, R., Hu, S., Tian, R., Huang, H., Wu, L., Lin, H., Sun, Y., Zhao, L., 2013b. An unstructured-grid, finite-volume community ocean model FVCOM user manual, 3rd edition. SMAST/UMASSD Technical Report-13-0701, University of Massachusetts-Dartmouth, p. 404.

Chen, C., Beardsley, R.C., Hu, S., Xu, Q., Lin, H., 2005. Using MM5 to hindcast the ocean surface forcing fields over the Gulf of Maine and Georges Bank region. J. Atmos Oceanic Technol. 22 (2), 131–145. https://doi.org/10.1175/JTECH-1682.1.

Chen, C., Gao, G., Qi, J., Proshutinsky, A., Beardsley, R.C., Kowalik, Z., Lin, H., Cowles, G., 2009. A new high-resolution unstructured grid finite volume Arctic Ocean model (AO-FVCOM): an application for tidal studies. J. Geophys. Res.-Oceans 114, C08017. https://doi.org/10.1029/2008JC004941.

Chen, C., Gao, G., Zhang, Y., Beardsley, R.C., Lai, Z., Qi, J., Lin, H., 2016. Circulation in the Arctic Ocean: Results from a high-resolution coupled ice-sea nested Global-FVCOM and Arctic-FVCOM system. Prog. Oceanogr. 141, 60–80. https://doi.org/10.1016/j.pocean.2015.12.002.

Davis, C., Wang, W., Chen, S.Y., Chen, Y.S., Corbisero, K., Demaria, M., Dudhia, J., Holland, G., Klemp, J., Michalakes, J., Reeves, H., Routunno, R., Syder, C., Xiao, Q. N., 2008. Prediction of landfalling hurricanes with the Advanced Hurricane WRF model. Mon. Weather Rev. 136, 1990–2005. https://doi.org/10.1175/2007MWR2085.1.

Edson, J.B., et al., 2013. On the exchange of momentum over the open ocean. J. Phys. Oceanogr. 43, 1589–1610. https://doi.org/10.1175/JPO-D-12-0173.1.

Emanuel, K., 1986. An air-sea interaction theory for tropical cyclones. Part I: steady-state maintenance. J. Atmos. Sci. 43 (6), 585–604.

Emanuel, K., 2003. Tropical cyclones. 31, 75-104, https://doi.org/10.1146/annurev.earth.31.100901.141259.

Fairall, C.W., Bradley, E.F., Rogers, D.P., Edson, J.B., Young, G.S., 1996. Bulk parameterization of air-sea fluxes for tropical ocean-global atmosphere coupled-ocean atmosphere response experiment. J. Geophys. Res.-Oceans 101, 3747–3764.

Fairall, C.W., Bradley, E.F., Hare, J.E., Grachev, A.A., Edson, J.B., 2003. Bulk parameterization of air-sea fluxes: updates and verification for the COARE algorithm. J. Climate 16, 571–591.

Fierro, A.O., Rogers, R.F., Marks, F.D., Nolan, D.S., 2009. The impact of horizontal grid spacing on the microphysical and kinematic structures of strong tropical cyclones simulated with the WRF-ARW model. Mon. Weather Rev. 137, 3717–3743. https://doi.org/10.1175/2009MWR2946.1.

Frank, W.M., 1987. Tropical cyclone formation. Global View of Tropical Cyclones, R.L. Elsberry, (Ed.), Office of Naval Research, 53–90.

Gao, G., Chen, C., Qi, J., Beardsley, R.C., 2011. An unstructured grid, finite-volume sea ice model: Development, validation, and application. J. Geophys. Res.-Oceans 116, C00D04. https://doi.org/10.1029/2010JC006688.

Gilhousen, D. B., Hervey, R., 2001. Improved estimates of swell from moored buoys. In: Proceedings of the Fourth International Symposium WAVES 2001, ASCE, Alexandria, VA, pp. 387–393.

Glenn, S.M., Miles, T.N.,Seroka, G.N.N., Xu, Y., Forney, R.K., Yu, F., Roarty, H., Schofield, O., Kohut, J., 2016. Stratified coastal ocean interactions with tropical cyclones, Nat. Commun. 7, 10887, https://doi.org/10.1038/ncomms10887.

Gopalakrishnan, S.G., Surgi, N., Tuleya, R., Janjić, Z., 2006. NCEP's Two-way-Interactive-Moving-Nest NMM-WRF modeling system for Hurricane Forecasting, 27th Conference on Hurricanes and Tropical Meteorology, Monterey, CA, American Meteorological Society, Ar. A. 7, http://ams.confex.com/ams/pdfpapers/107899.pdf.

Greenpan, H., 1968. The Theory of Rotating Fluids. Cambridge Univ. Press, Cambridge UK, p. 327.

Huang, P., Sanford, T.B., Imberger, J., 2009. Heat and turbulent kinetic energy budgets for surface layer cooling induced by the passage of Hurricane Frances. J. Geophys. Res.-Oceans 114, C12023. https://doi.org/10.1029/2009JC005603.

Jacob, S.D., Shay, L.K., Mariano, A.J., Black, P.G., 2000. The 3D oceanic mixed layer response to Hurricane Gilbert. J. Phys. Oceanogr. 30, 1407–1429. https://doi.org/10.1175/1520-0485(2000)030<1407:TOMLRT>2.0.CO;2.

Li, C.Y., 1988. Actions of typhoon over the western Pacific (including the South China Sea) and EI Nino. Adv. Atmos. Sci. 5 (1), 107–116.

Li, S., Chen, C., Wu, Z., Beardsley, R.C., Li, M., 2020a. Impacts of oceanic mixing on hurricanes: a simulation experiment with Hurricane Sandy. J. Geophys. Res.-Oceans, 125, e2019JC015851. https://doi.org/10.1029/2019JC015851.

Li, S., Chen, C., Wu, Z., Qi, J., Beardsley, R.C., Dong, W., Xu, D., 2020b. A coupled FVCOM-WRF model: applications for hurricane and typhoon simulations. Abstract. The 2020 Ocean Science Meeting, 16–21 February, 2020, Dan Diego, CA, USA.

Mellor, G.L., Yamada, T., 1982. Development of a turbulence closure model for geophysical fluid problem. Rev. Geophys. Space. Phys. 20, 851–875.

Moeng, C.H., Dudhia, J., Klemp, J., Sullivan, P., 2007. Examining two-way grid nesting for large eddy simulation of the PBL using the WRF model. Mon. Weather Rev. 135, 2295–2311.

Mooney, P., Gill, D.O., Mulligan, F.J., Bruyère, C.L., 2016. Hurricane simulation using different representations of atmosphere–ocean interaction: the case of Irene (2011). Atmos. Sci. Lett. 17 (7), 415–421. https://doi.org/10.1002/asl.673.

Neumann, C., 1993. Global overview. In Global Guide to Tropical Cyclone Forecasting WMO/TD-560, ed. G. J. Holland, pp. 3.1–3.46. Geneva: World Meteorol. Org.

Pollard, R.T., Rhines, P.B., Thompson, R.O., 1973. The deepening of the wind-mixed layer. Geophys. Astrophys. Fluid Dyn. 3, 381–404. https://doi.org/10.1080/03091927208236105.

Price, J.F., Weller, R.A., Pinkel, R., 1986. Diurnal cycling: observations and models of the upper ocean response to diurnal heating, cooling, and wind mixing. J. Geophys. Res.-Oceans 91, 4811–4827.

Qiu, W.Y., Ren, F., Wu, L.G., Chen, L.S., Ding, C.C., 2019. Characteristics of tropical cyclone extreme precipitation and its preliminary causes in Southeast China. Meteorol. Atmos. Phys. 31 (3), 613–626.

Schlichting, H., 1979. Boundary-Layer Theory, Transl. by J. Kestin. 7th ed, McGraw-Hill Series in Mechanical Engineering. New York-St. Louis-San Francisco-Auckland-Bogotà-Düsseldorf-Johannesburg-London-Madrid-Mexico-Montreal-New Delhi-Panama-Paris-São Paulo-Singapore-Sydney-Tokyo-Toronto, McGraw-Hill Book Company, p. 817.

Skamarock, W.C., et al., 2008. A description of the Advanced Research WRF version 3, NCAR Tech. Note NCAR/TN-475+STR, p. 125, https://doi.org/10.5065/D68S4MVH.

Wang, Z.X., He, S.X., 1979. A tropical cyclones developed from a South China Sea front depression. In: Typhoon and Tropical Circulation, Institute of Atmosphere Physics (Ed.), Science Press, vol. 8, pp. 52–65.

Wang, G.H., Su, J., Ding, Y.H., Chen, D., 2007. Tropical cyclone genesis over the South China Sea. J. Mar. Syst. 68, 318–326.

Warner, J.C., Armstrong, B., He, R., Zambon, J.B., 2010. Development of a coupled ocean–atmosphere–wave–sediment transport (COAWST) modeling system. Ocean Model. 35 (3), 230–244. https://doi.org/10.1016/j.ocemod.2010.07.010.

Yablonsky, R.M., Ginis, I., 2009. Limitation of one-dimensional ocean models for coupled hurricane-ocean model forecasts. Mon. Weather Rev. 137, 4410–4419. https://doi.org/10.1175/2009 MWR2863.1.

Yi, X., 2020. Preliminary establishment of temperature and salinity dataset in the China Sea and analysis of climate change characteristics in the Kuroshio region, Master Thesis of the Sun Yat-sen University, Technical Report No.17214834, p. 65.

Yi, X., Dong, W., Lee, S., Li, Y., Xu, D., Wang, Z., 2020. Sea temperature variations and causes in the Kuroshio area in the East China Sea. Marine Forecasts (in Chinese with English abstract), in press.

Zhang, Y., Chen, C., Beardsley, R.C., Guo, G., Lai, Z., Curry, B., Lee, G.M., Lin, H., Qi, J., Xu, Q., 2016a. Studies of the Canadian Arctic Archipelago water transport and its relationship to basin-local forcings: results from AO-FVCOM. J. Geophys. Res.-Oceans 121 (6), 4392–4415. https://doi.org/10.1002/2016JC011634.

Zhang, Y., Chen, C., Beardsley, R.C., Gao, G., Qi, J., Lin, H., 2016b. Seasonal and interannual variability of the Arctic sea ice: a comparison between AO-FVCOM and observations. J. Geophys. Res.-Oceans 121 (11), 8320–8350. https://doi.org/10.1002/2016JC011841.

Zhang, Y., Chen, C., Beardsley, R.C., Perrie, W., Gao, G., Zhang, Y., Qi, J., Lin, H., 2020. Applications of an unstructured grid surface wave model (FVCOM-SWAVE) to the Arctic Ocean: the interaction between ocean waves and sea ice. Ocean Model. 145, 101532 https://doi.org/10.1016/j.ocemod.2019.101532.

Zou, X., Xiao, Q., 2000. Studies on the initialization and simulation of a mature hurricane using a variational bogus data assimilation scheme. J. Atmos. Sci. 57 (6), 836–860. https://doi.org/10.1175/1520-0469(2000)057<0836:SOTIAS>2.0.CO;2.